

M dwarf spectral indices at moderate resolution: accurate T_{eff} and $[\text{Fe}/\text{H}]$ for 178 southern stars[★]

Ellen Costa-Almeida,^{1,2} † Gustavo F. Porto de Mello,¹ Riano E. Giribaldi,³ Diego Lorenzo-Oliveira,⁴ Maria L. Ubaldo-Melo¹

¹Observatório do Valongo, Universidade Federal do Rio de Janeiro, Ladeira do Pedro Antônio 43, 20080-090 Rio de Janeiro, RJ, Brazil

²Observatório Nacional/MCTI, Rua General José Cristino 77, 20921-400 Rio de Janeiro, RJ, Brazil

³Nicolaus Copernicus Astronomical Center, Polish Academy of Sciences, Bartycka 18, 00-716, Warsaw, Poland

⁴Universidade de São Paulo, Departamento de Astronomia do IAG/USP, Rua do Matão 1226, Cidade Universitária, 05508-900 São Paulo, SP, Brazil

Accepted 2021 September 28. Received 2021 September 28; in original form 2021 May 11

ABSTRACT

We present a spectroscopic and photometric calibration to derive effective temperatures T_{eff} and metallicities $[\text{Fe}/\text{H}]$ for M dwarfs, based on a Principal Component Analysis of 147 spectral indices measured off moderate resolution ($R \sim 11,000$), high S/N (> 100) spectra in the $\lambda\lambda$ 8390–8834 region, plus the J–H color. Internal uncertainties, estimated by the residuals, are 81 K and 0.12 dex, respectively, for T_{eff} and $[\text{Fe}/\text{H}]$, the calibrations being valid for 3050 K $< T_{\text{eff}} < 4100$ K and $-0.45 < [\text{Fe}/\text{H}] < +0.50$ dex. The PCA calibration is a competitive model-independent method to derive T_{eff} and $[\text{Fe}/\text{H}]$ for large samples of M dwarfs, well suited to the available database of far-red spectra. The median uncertainties are 105 K and 0.23 dex for T_{eff} and $[\text{Fe}/\text{H}]$, respectively, estimated by Monte Carlo simulations. We compare our values to other works based on photometric and spectroscopic techniques and find median differences 75 ± 273 K and 0.02 ± 0.31 dex for T_{eff} and $[\text{Fe}/\text{H}]$, respectively, achieving good accuracy but relatively low precision. We find considerable disagreement in the literature between atmospheric parameters for stars in common. We use the new calibration to derive T_{eff} and $[\text{Fe}/\text{H}]$ for 178 K7–M5 dwarfs, many previously unstudied. Our metallicity distribution function for nearby M dwarfs peaks at $[\text{Fe}/\text{H}] \sim -0.10$ dex, in good agreement with the RAVE distribution for GK dwarfs. We present radial velocities (internal precision 1.4 km/s) for 99 objects without previous measurements. The kinematics of the sample shows it to be fully dominated by thin/thick disk stars, excepting the well-known high-velocity Kapteyn’s star.

Key words: stars: fundamental parameters – stars: low-mass – techniques: spectroscopic – stars: abundances – Galaxy: solar neighborhood

1 INTRODUCTION

M dwarfs represent more than 70% in number and about 40% of the stellar mass content of the Galaxy (Kirkpatrick et al. 2012), ranging from 0.08 M_{\odot} to 0.6 M_{\odot} – even though an extension towards even less massive objects is possible if they are very young, see Sahlmann et al. (2021) – and, along with the fact that they have main-sequence lifetimes exceeding the Hubble time, they are fundamental assets towards a realistic understanding of the formation, structure and chemodynamical evolution of the Galaxy. Because of their very high number density, they are attractive targets in the search for exoplanets, especially rocky planets, since the sensitivity of the

transit and radial-velocity techniques performs better for higher planet-to-star mass and radius ratios. Estimates show that there are at least 3 planets per M dwarf (Tuomi et al. 2019) and that smaller planets are more likely to be formed around smaller stars (e.g., Bonfils et al. 2013; Dressing & Charbonneau 2013; Tuomi et al. 2014). Therefore, there is an urge for accurate, extensive and homogeneous stellar properties of M dwarf stars.

The precise estimation of atmospheric parameters of M dwarfs is a theoretical and observational challenge, especially when compared to the classical model atmospheres methods applied for solar-type stars, which are very precise and accurate. M dwarfs are so cool that diatomic and triatomic molecules can survive in their atmospheres, filling the spectra with many absorption bands and making it very difficult, and often impossible, to identify the continuum itself and individual absorption lines. Because of this, most of the techniques used to derive atmospheric parameters, particularly effective temperature and metallicity (hereafter, T_{eff} and $[\text{Fe}/\text{H}]$,

[★] Based on observations collected at Observatório do Pico dos Dias (OPD), operated by the Laboratório Nacional de Astrofísica, MCTI, Brazil.

† Present Address: Observatório Nacional/MCTI, Rio de Janeiro, RJ, Brazil. Email Addresses: ellenalmeida@on.br (ECA); gustavo@astro.ufrj.br (GFPdM).

respectively), are based on calibrations using photometric colors (e.g., Bonfils et al. 2005, Casagrande et al. 2008, Neves et al. 2012) or spectral indices (e.g., Rojas-Ayala et al. 2012, Mann et al. 2013a, Neves et al. 2014, Newton et al. 2015, López-Valdivia et al. 2019).

Regarding T_{eff} , interferometry has been used to derive *practically model-independent* precise estimates for bright and nearby M dwarfs with uncertainties smaller than 100 K by using relationships between stellar radius and T_{eff} (e.g., Boyajian et al. 2012; von Braun et al. 2014). However, there is only a limited number of stars with radii measured by this technique, especially in the southern hemisphere (e.g., Ségransan et al. 2003; Rabus et al. 2019). When we consider differences between recent T_{eff} determinations, we find offsets reaching up to 300 K between model-dependent studies. Our lack of comprehension of interiors and atmospheres of almost fully convective low-mass stars, together with our incomplete database of atomic and molecular transitions, are mainly responsible for the discrepancies observed in the literature. Therefore, studies that use interferometric T_{eff} estimations as calibrators offer advantages in accuracy and should be preferred for the systematic derivation of atmospheric parameters from indirect methods. We have recently showed the competitiveness of line indexes to derive accurate and precise atmospheric parameters for solar-type stars (e.g., Ghezzi et al. 2014, Giribaldi et al. 2019) as long as a suitable sample of calibrating stars is employed and systematic errors are carefully checked and accounted for. Additional efforts to extend this technique to lower T_{eff} domain, thus, appear to be fully warranted.

Regarding $[\text{Fe}/\text{H}]$ ¹, a common practice is to employ wide physical binaries systems of FGK + M dwarf by assuming that the composition of the hotter star, which usually has a precise $[\text{Fe}/\text{H}]$ determination with typical uncertainties around 0.07 dex, can be extrapolated to its cooler companion (e.g., Neves et al. 2012; Mann et al. 2013b, 2015; Montes et al. 2018), although considering the high frequency of planets around M dwarfs, planet accretion scenarios can change the original composition of the star and should be considered with caution (e.g., Teske et al. 2015; Oh et al. 2018). Moreover, typical uncertainties around 0.10 dex are presently achievable using spectral features in the NIR (e.g., Rojas-Ayala et al. 2012; Mann et al. 2013a; Neves et al. 2014) and around 0.20 dex using photometric calibrations (e.g., Bonfils et al. 2005; Neves et al. 2012; Newton et al. 2014), even though the agreement of values between methods is less than perfect. We refer the reader to Lindgren et al. (2016) who reported differences of ~ 0.6 dex for individual stars comparing different calibrations.

Accurate $[\text{Fe}/\text{H}]$ determinations are essential for a better understanding of the composition of exoplanets. Nowadays, it is widely established that, on average, metal-rich FGK stars have a higher frequency of planets (e.g., Santos et al. 2004; Valenti & Fischer 2005; Ghezzi et al. 2018). However, recent studies are finding evidence that this trend is also true for host M dwarfs (e.g., Hobson et al. 2018). Thus, the previous knowledge of $[\text{Fe}/\text{H}]$ is important to focus the search for interesting planet-hosting M dwarfs for future direct observations of their planets with upcoming instrumentation such as GMT, JWST and LUVOIR.

In our work we present accurate model-independent T_{eff} and $[\text{Fe}/\text{H}]$ determinations for 178 southern M dwarf stars in the solar neighbourhood. We explore the equivalent widths (hereafter, EW) of 147 spectral indices in the far red together with $J - H$ color to derive the Principal Components of the Principal Component Anal-

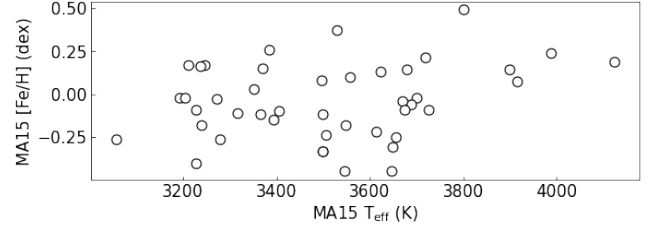


Figure 1. Distribution of the atmospheric parameters of the calibration stars. Values taken from Mann et al. 2015.

ysis (hereafter, PCA). Our atmospheric parameter scale is calibrated with 44 stars from Mann et al. 2015, who used more than 20 stars with interferometric T_{eff} determinations as calibrators. In Sect. 2 we describe the sample selection and define the calibration stars. In Sect. 3 we describe the characteristics of the spectroscopic observations of the 178 program stars, the measurement of radial velocities, the calculation of the stellar space velocities and Galactic orbits, and the procedure for normalizing the continuum. In Sect. 4 we describe the line index system, its definition criteria and associated errors. In Sect. 5 we present the calibrations for T_{eff} and $[\text{Fe}/\text{H}]$. In Sect. 6 we describe the Monte Carlo simulations performed to gauge the errors of the calibrations and present the final atmospheric parameters. We also compare our results to previously published values derived using other techniques. In Sect. 7 we analyse the Galactic orbits of the M dwarfs and associate them to the Galactic substructures. In Sect. 8 we summarize our conclusions.

2 SAMPLE SELECTION

This project started on 2007, as a pilot, initially targeting a sample of 94 stars selected from the Hipparcos Catalog (Perryman et al. 1997) which, by that time, had the most precise parallaxes available. The sample is volume limited ($\pi > 100$ mas, i.e., $d < 10$ pc) and emphasized stars brighter than $V \sim 11$ mag. We observed this initial sample on 5 observing runs, from 2007 to 2011. The observations were resumed in 2016 and the sample was considerably expanded by adding stars from Winters et al. (2015) having trigonometric distances $d \leq 20$ pc and $V \leq 13$ mag. By the end of 6 additional observing runs from 2017 to 2018, we observed in total 178 southern ($\delta \lesssim +20$) K7V-M5.5V stars.

We completed our observation runs having 44 stars in common with Mann et al. (2015) (hereafter, MA15), who derived T_{eff} by comparing optical spectra with PHOENIX atmosphere models and obtained $[\text{Fe}/\text{H}]$ from EWs of Ca and Na atomic lines in the NIR (Mann et al. 2013a and Mann et al. 2014). These objects are henceforth referred to as “calibration stars” and the atmospheric parameter space they cover is shown in Figure 1, 3056 to 4124 K and -0.45 to $+0.49$ dex for T_{eff} and $[\text{Fe}/\text{H}]$, respectively. Although our calibration sample has a bias for stars with $T_{\text{eff}} > 3800$ K, in the sense that hotter stars are all metal-rich, we have kept these K stars in common with MA15 to investigate if the spectral index method would be amenable to extrapolation.

¹ Hereafter defined as $[\text{Fe}/\text{H}]_{\star} = \log\left(\frac{N_{\text{Fe}}}{N_{\text{H}}}\right)_{\star} - \log\left(\frac{N_{\text{Fe}}}{N_{\text{H}}}\right)_{\odot}$, where N_{Fe} and N_{H} are the number density of Fe and H atoms, respectively.

Table 1. Average exposure times and approximate nominal S/N ratios for the averaged spectra.

V (mag)	Exposure time (s)	Nominal S/R
$V \leq 10.0$	3×600	150
$10.0 < V \leq 10.5$	3×900	150
$10.5 < V \leq 11.5$	4×900	150
$11.5 < V \leq 12.0$	4×900	150
$12.0 < V \leq 12.5$	5×900	100
$12.5 < V \leq 13.0$	6×1200	100

3 OBSERVATIONS AND REDUCTION

3.1 Coudé spectroscopy

We used the coudé spectrograph fed by the 1.60m Perkin-Elmer telescope of Observatório do Pico dos Dias (OPD, Brazópolis, Brazil), operated by Laboratório Nacional de Astrofísica (LNA/CNPq). The old (2007 to 2012) and new (2017 to 2018) data were obtained using two different CCDs, yet possessing very similar specifications, both having 2048 pixels and $13.5 \mu\text{m}/\text{pixel}$. The slit width was adjusted to $500 \mu\text{m}$ to give a 3-pixel resolving power $R \approx 11000$ and a 600 l/mm diffraction grating was employed in the first order, obtaining $0.25 \text{ \AA}/\text{pixel}$. We used a yellow RG 610 filter to block contamination from the second order. The spectral region is centered at 8650 \AA , with a spectral coverage of 500 \AA (8370 to 8870 \AA). One clear advantage of this range as compared to bluer regions is the much diminished line blanketing, making the local continuum much more accessible, at least for the hotter subtypes. This fact lends more credence to the spectral indices, which are probably reflecting true physical absorption more realistically. Our sample stars were sufficiently faint for exposure times to often be substantial.

We divided the exposure times based on V magnitude values to achieve nominal S/N greater than 100 for all spectra (see Table 1). These stars do not have clear continuum windows free of absorption lines to directly estimate the continuum fluctuations, so we estimated the nominal S/N ratios by means of Poissonian photon statistics probably slightly overestimating the actual S/N ratios. Sample spectra of cool, intermediate and hot M dwarfs are shown in Figure 2, for average quality spectra. The data reduction was carried out by standard techniques with a Python script calling IRAF² tasks through Pyraf.

3.2 Radial velocities and Galactic kinematic parameters

Doppler shift correction is a standard procedure in data reduction, but since these stars were poorly represented in RV catalogs up until Gaia Data Release 2 (Soubiran et al. 2018, Gaia DR2), we are presenting our values of radial velocity.

We selected 10 relatively isolated spectral lines spread along the full spectral coverage and used the central wavelengths values at rest from the version 5.7 of the NIST Standard Reference Database 78³ (see Table 2). For each observing run, we selected a hot (K, M0 or M1) and a cool (M2, M3 or M4) star to be our template spectra and manually measured the observed central wavelengths (λ_{obs}) of the 10 lines using the *splot* IRAF task. We used the mean value

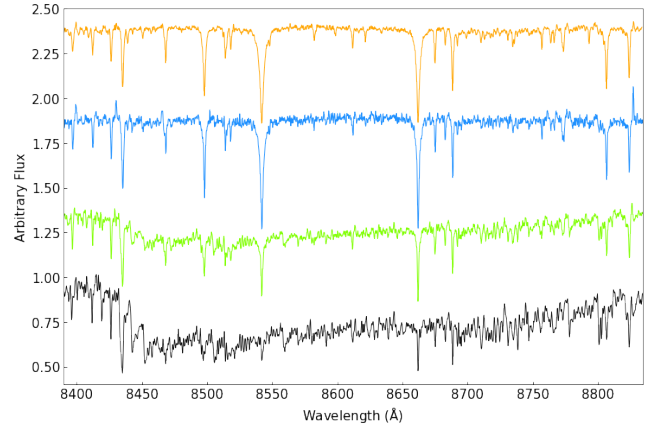


Figure 2. Sample spectra of hot, intermediate and cool M dwarfs for average quality spectra. From top to bottom we show HIP 40239 (M0V, orange line), HIP 72511 (M1.5V, blue line), HIP 53020 (M4V, green line) and HIP 70890 (M5.5V, black line) having nominal S/N of 190, 160, 150 and 180, respectively.

Table 2. Atomic lines used for the Doppler correction.

λ_{central}	Element
8468.407	Fe I
8611.803	Fe I
8621.600	Fe I
8633.956	Ca I
8682.987	Ti I
8688.625	Fe I
8757.187	Fe I
8763.966	Fe I
8806.575	Mg I
8824.221	Fe I

and the standard deviation as final observed velocity and associated error, respectively. We used the task *dopcor* for the Doppler shift correction and obtained spectra at rest (template spectra).

Considering that molecular absorption changes dramatically for different M spectral subtypes, turning a M4V spectrum really different from a M0V, using hot/cool template spectra was extremely important for performing a Fourier cross-correlation on the input list of objects and template spectra. This procedure produced for the whole sample relative and heliocentric velocities and the associated error. The overall internal precision, estimated from the median of our velocity uncertainties, is 1.40 km/s . We compared our results with Gaia Data Release 2 radial velocities and found a mean difference of $-2.42 \pm 5.92 \text{ km/s}$ for 79 stars in common (see Figure 3). A possible slight underestimation of our RV values with respect to Gaia DR2 is suggested, but without clear statistical significance regarding the internal errors of both. We thus provide new RVs for 99 stars without any previous data from Gaia and the RV results are given in Table A2.

We integrated stellar orbits running the code GalPot⁴ (McMillan 2017) with which we obtained the integrals of motion: orbital energy and the angular momentum component perpendicular to the Galactic plane L_z . For the calculations, we adopted the best-fit Galactic potential model of (McMillan 2017) and used the Galactic

² Image Reduction and Analysis Facility (IRAF) is distributed by the National Optical Astronomical Observatories (NOAO), which is operated by the Association of Universities for Research in Astronomy (AURA), Inc., under contract to the National Science Foundation (NSF).

³ <https://www.nist.gov/pml/atomic-spectra-database>

⁴ <https://github.com/PaulMcMillan-Astro/GalPot>

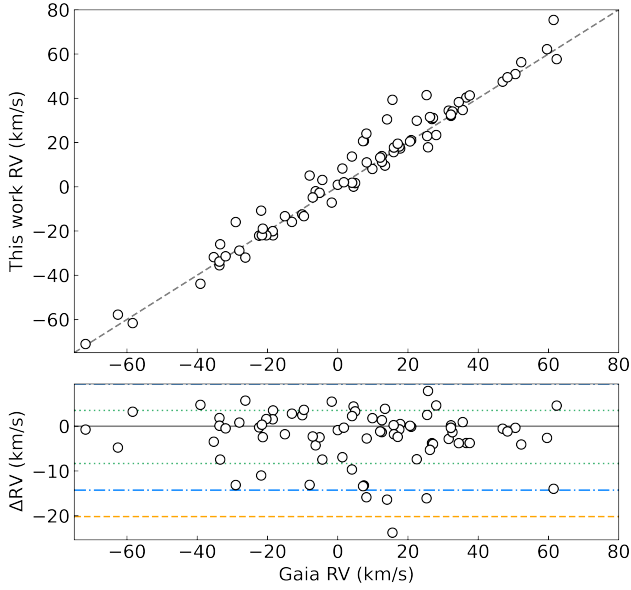


Figure 3. Upper panel: Comparison between radial velocities from this work for 79 stars in common with measured RV velocities on Gaia Data Release 2. The dashed grey line represents equality. Bottom panel: RV comparison (Gaia-this work) between Gaia and this work. The differences have a RMS scatter of 5.92 km/s and a zero-point difference of -2.42 km/s. For this sample, the median errors of Gaia radial velocities is 0.245 km/s and ours is 1.243 km/s. The grey solid line represents the zero, green dotted lines are $\pm 1\sigma$, blue dash-dotted lines are $\pm 2\sigma$ and orange dashed line represents 3σ of the distribution. The four high residuals ($> 2\sigma$) are identified as HIP67155, HIP 439, HIP 65859 and HIP 114046 having radial velocities of 39.3 ± 1.3 , 41.1 ± 1.4 , 30.5 ± 1.2 and 34.1 ± 1.5 km/s, respectively. None of them are known binary systems, and we note that HIP 114046 has two confirmed planets (Jeffers et al. 2020).

space-velocity components ($R_{\text{Gal}}, \phi, Z - U, V_{\phi}, W$) derived from the radial velocities in Table A2, and the coordinates, parallaxes, and proper motions from the Gaia EDR3 catalog (Gaia Collaboration et al. 2021). The frame transformations were performed using Astropy (Astropy Collaboration et al. 2013, 2018) and PyAstronomy routines (Czesla et al. 2019) adopting the Galactocentric solar position in McMillan (2017) and the solar velocity respect to the local standard of rest determined by Schönrich et al. (2010). The parameters above will be used in Sect. 7 to analyse the dynamic distribution of the M dwarfs in the Galactic substructures. For comparison purposes, the same procedure was also applied to 5000 random stars from the Gaia DR2 catalog restricted to $\pi > 10$ mas with precisions better than 10% ($\sigma_{\pi}/\pi < 0.1$) and available radial velocities.

3.3 Normalization

We divided sample stars into hot (K dwarfs, M0V and M1V) and cool (higher than M2V) groups. The pseudo continuum was well defined for the hot group and thus a low order polynomial function sufficed to establish the local continuum. The absorption from molecules, specially TiO bands, is responsible for a substantial depression in the pseudo continuum of cooler stars. We therefore, after some tests, simply connected the two highest local continuum points with a straight line (usually 8400 Å and 8850 Å), considering these as the only local continuum points (see Figure 2).

4 LINE INDEX DEFINITION AND MEASUREMENT

Spectral index is a region of the spectrum which contains a group of atomic and/or molecular lines that can not be individually distinguished but, as a group, are sensible to the variation of one or more atmospheric parameters. Its definition is made based on a visual inspection of the spectrum, i. e., there is no need to know about the physical properties of the star beforehand. Furthermore, this technique does not depend on models of internal structure or stellar atmosphere, turning it directly applicable to the spectrum without the necessity to stipulate hypothesis nor make previous interpretations in respect to the definition of the indices.

4.1 Definition of the indices

The definition of the spectral indices was made based on a visual inspection of the spectra of 4 representative stars of spectral subtypes that compose our sample: M0V, M2V, M4V and M5.5V. We over-plotted these spectra, looked for regions with a clear similar variation of the flux in the four of them and used the initial and final wavelengths of the coolest star to stipulate the limits to each group of lines (see Figure 4). We used all the spectrum coverage to define the indices, i. e., no region was ignored and there is no region in common between two indices. We defined 170 indices from 8390.17 to 8834.47 Å (see Table A1).

The spectral indices in this region are dominated by neutral iron-peak species (such as 14 Fe I, 19 Ti I and 1 Mg I lines), ionized species (such as 3 Ca II lines) and molecular bands (such as 2 TiO, 1 FeH and 1 VO bands). For a detailed description of the spectral lines in this spectral range we refer the reader to Reiners et al. (2018). Besides, taking into consideration the possible chromospheric effects in the spectrum caused by the magnetic activity of the star, we did not use the indices constituted by the Ca II triplet lines ($i42$, $i60$ and $i105$) because these lines can have a meaningful chromospheric filling-in (e.g., Lorenzo-Oliveira et al. 2016), thereby polluting any correlation with T_{eff} and $[\text{Fe}/\text{H}]$.

4.2 Sanity check and associated errors

We verified if the indices had an appropriate physical behavior to decide which ones would be used in the next step. We certified the sensitivity of each index with respect to both T_{eff} and $[\text{Fe}/\text{H}]$ for the calibration sample by estimating the Pearson correlation coefficient (see Figure 5). The correlation visibly reduces as the wavelength increases, except for the initial part of the spectra which doesn't present a clear pattern on both graphics. This may be due to the presence of strong telluric absorption lines in this region (e.g., Matheson et al. 2000) for stars observed (9 calibration stars have more than one observation) on nights in which humidity was particularly high. In light of this, we decided not to use the first 19 indices for our analysis.

The consistency and repeatability of the EWs is extremely important for our method. The percent variation of the EW measurement will represent the associated error for each index. Between all observed stars, 41 had more than one spectrum. We calculated the relative error of each index of each star ($\sigma_{\star}^{\text{rel}}$)

$$\sigma_{\star}^{\text{rel}} = \left[\frac{\sigma_{\text{EW}_{i20}}^{\text{EW}}}{\text{med}(\text{EW}_{i20})} \quad \cdots \quad \frac{\sigma_{\text{EW}_{i170}}^{\text{EW}}}{\text{med}(\text{EW}_{i170})} \right]. \quad (1)$$

We obtained a distribution of 41 relative errors for each one of the 147 spectral indices. We assume that the final relative error is the

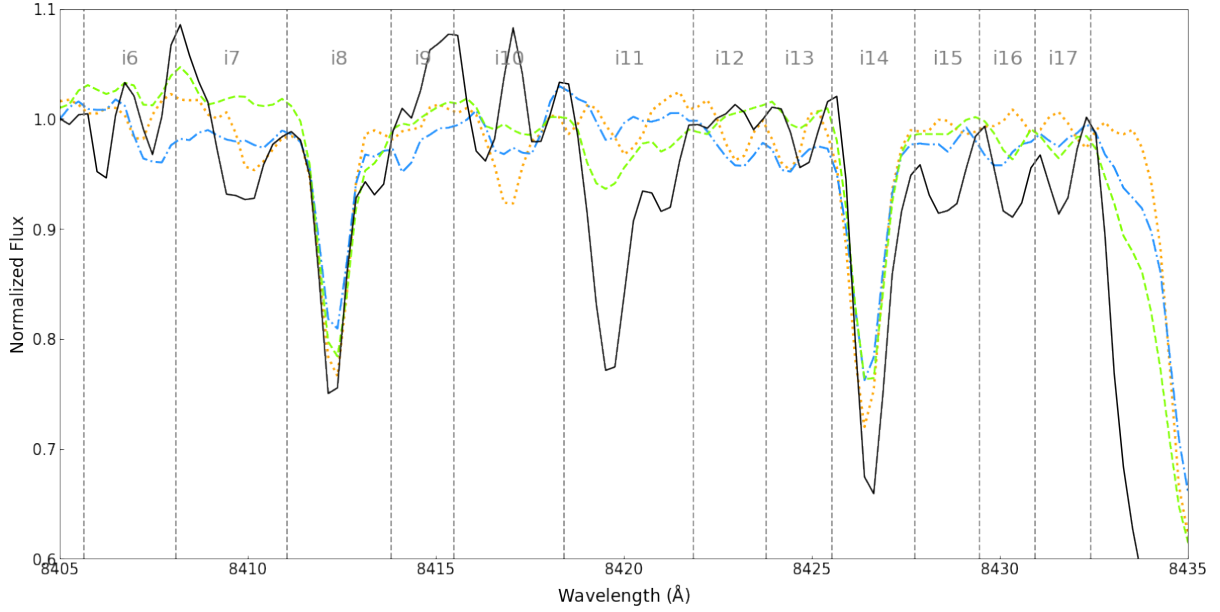


Figure 4. Example of the definition of the spectral indices. Each index is represented as i followed by a number (from 1 to 170) for increasing central wavelength. The dashed vertical grey lines represent the initial and final limits of each index. HIP 99701 (M0V) is the orange dotted line, HIP 51317 (M2V) is the blue dash-dotted line, HIP 87937 (M4V) is the green dashed line and Proxima Centauri (M5.5V) is the black solid line.

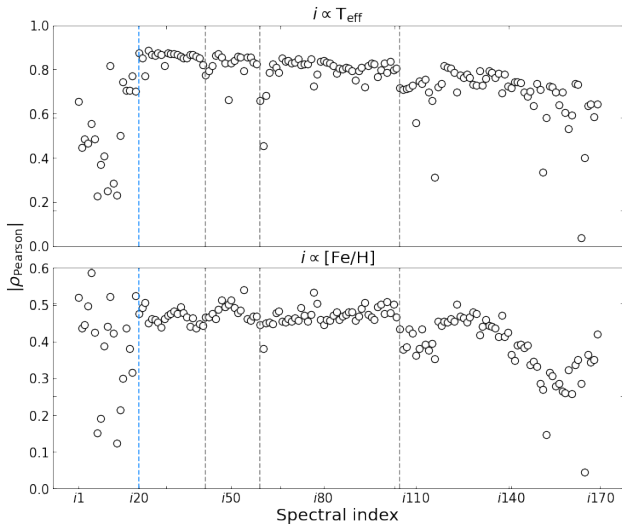


Figure 5. Module of the Pearson correlation coefficient for each index with respect to T_{eff} (upper panel) and $[\text{Fe}/\text{H}]$ (lower panel). The blue dotted line indicates the 20th index (see text) and the 3 grey dashed lines indicate the Ca II triplet lines.

median of the distribution of each index

$$\sigma^{\text{rel}} = [\text{med}(\sigma_{i20}^{\text{rel}}) \quad \dots \quad \text{med}(\sigma_{i170}^{\text{rel}})]. \quad (2)$$

We found that the EWs are stable with a mean variation of $11 \pm 8\%$ (1σ). Only $i149$ and $i157$ show relative errors greater than the 3σ cut, respectively 49% and 47%. We estimate how these relative errors can modify our results in the next Section, but, for now, we remark that the final contribution of each index will be diluted within the Principal Components, reducing their particular impact.

The initial and final wavelengths and final relative uncertainties of all the spectral indices can be found in Table A1.

5 METHODS

Towards the goal of reducing the total number of variables to work with, turning them independent from one another and not over fitting our data, we use the Principal Component Analysis (PCA), which is a technique of feature extraction. In addition, it should be noted that PCA is a model-independent mathematical tool, but since it finds the best components to replicate the trend observed in the calibration sample atmospheric parameters, it also replicates its offsets and their model dependence. Our work follows very closely the methods exposed by Giribaldi et al. (2019) and thus a full discussion is unwarranted. A short description of the variables used to create the PCs and the regression strategy is given below.

5.1 Incorporating 2MASS photometry

The initial approach was to create the PCs based exclusively on the 147 spectral indices – a purely spectroscopic approach. We found a great correlation between T_{eff} and the first 3 PCs, i.e., the components that exhibit the 3 greatest variances of our data. This result was expected since T_{eff} determines most of the spectrum shape. However, the $[\text{Fe}/\text{H}]$ presented a poor correlation between the first 7 PCs – which were responsible for 98.7% of the total cumulative variance of the data –, so we investigated which colors had great correlations with $[\text{Fe}/\text{H}]$ by using the Pearson coefficient as a diagnostic. All stars observed have Gaia and 2MASS magnitudes, so we used colors having G , G_{RP} , J , H and K (see Table 3).

It is clear from Table 3 that $J - H$ and $J - K$ have the best correlations with $[\text{Fe}/\text{H}]$. Adding to that, we ran some tests to decide which and how many colors to use besides the 147 spectral indices. We found that it is not worth including colors to improve

Table 3. Pearson correlation between colors and atmospheric parameters.

Color	$\rho_{T_{\text{eff}}}$	$\rho_{[\text{Fe}/\text{H}]}$
$G - J$	-0.96	0.015
$G - H$	-0.93	0.124
$G - K$	-0.93	0.106
$G_{\text{RP}} - J$	-0.96	0.003
$G_{\text{RP}} - H$	-0.95	0.06
$G_{\text{RP}} - K$	-0.95	0.06
$J - H$	0.51	0.77
$J - K$	0.03	0.63
$H - K$	-0.59	-0.09

the correlation between T_{eff} and the PCs because the spectral indices have more than enough predictive power by themselves. By including them, we are only overdetermining T_{eff} and increasing the initial number of variables. Moreover, $J - H$ and $J - K$ together do not significantly change the correlations between $[\text{Fe}/\text{H}]$ and the PCs, $J - H$ being enough. Considering this, we created our principal components based on $J - H$ color and 147 spectral indices from 44 calibration stars – all having ‘A’ 2MASS quality flag for both J and H magnitudes. Ten calibration stars had more than one spectrum (57 spectra in total) but since adding variables with the same atmospheric parameters can create a bias around these values, we decided to use the mean EW of the indices of these stars. The color and spectral indices were standardized to take into account their different scales. The median and standard deviations of each variable used in the standardization procedure and the coefficients of the Principal Components created are listed in Table A2.

5.2 Calibrations by PCA

We explored the correlations between the first 5 principal components – which accounts for 97.8% of the total cumulative variance of the data – and the atmospheric parameters. The other higher principal components were discarded because they do not show significant correlations. T_{eff} has great correlations with PC1, PC2 and PC3 while $[\text{Fe}/\text{H}]$ is better described by PC3 and PC5. Although PC1 saturates approximately at 3800 K, in the same limit, PC2 and PC3 start to show a trend with effective temperature, helping to differentiate hotter stars. We used the best regressive model, i.e., smallest regressive error and greater degrees of freedom, to build calibrations for the atmospheric parameters as functions of the PCs (Equations 3 and 4).

$$T_{\text{eff}} = 3509.49(\pm 10.77) + 17.22(\pm 0.94)\text{PC1} - 31.51(\pm 3.99)\text{PC2} + 51.17(\pm 7.09)\text{PC3}; \quad (3)$$

$$[\text{Fe}/\text{H}] = -0.04(\pm 0.02) + 0.11(\pm 0.01)\text{PC3} + 0.07(\pm 0.02)\text{PC5}. \quad (4)$$

The internal uncertainties are 81 K and 0.115 dex and the Pearson correlations between the fitted and observed values are 0.96 and 0.82 for T_{eff} and $[\text{Fe}/\text{H}]$, respectively. Even though the correlation between $[\text{Fe}/\text{H}]$ and PC5 is not visually clear, adding PC5 to the regression increases the Pearson coefficient by 0.05 (0.77 to 0.82) and reduces the dispersion of the fitted values by 0.0415 (0.1562 to 0.1148). The same goes for T_{eff} where we find the Pearson coefficient increasing from 0.83 to 0.90 to 0.96, and the dispersion of the fitted values from 108.3 K to 99.49 K to 81.26 K for PC1, PC1+PC2 and PC1+PC2+PC3, respectively.

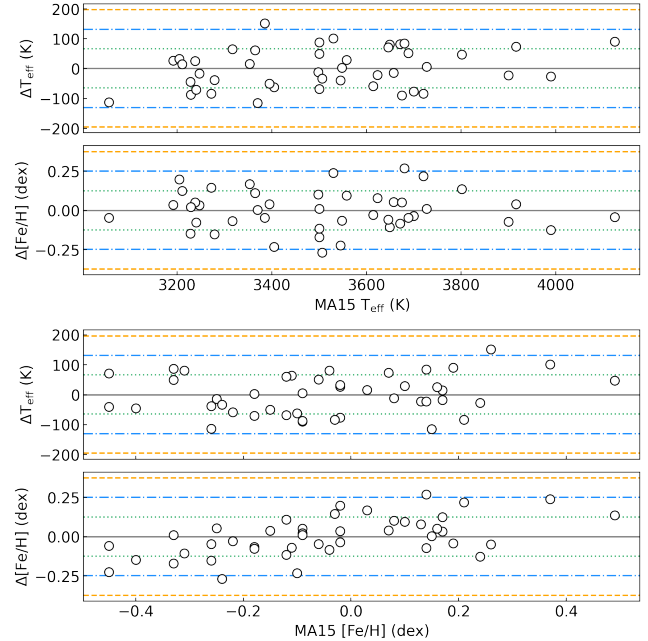


Figure 6. Residuals for both atmospheric parameters versus T_{eff} and $[\text{Fe}/\text{H}]$ from MA15 in the upper and bottom panels, respectively. T_{eff} and $[\text{Fe}/\text{H}]$ residuals have a RMS scatter of 65 K and 0.12 dex, respectively. Our residuals reach at most 2σ approximately for both atmospheric parameters, finding the worst cases around the richer and hotter K dwarf stars. The grey solid lines represent the zero, green dotted lines are $\pm 1\sigma$, blue dash-dotted lines are $\pm 2\sigma$ and orange dashed lines are $\pm 3\sigma$ of the distributions.

Table 4. Linear regressions between residuals and atmospheric parameters.

Y (Residual)	X (Parameter)	a_0 (t-value)	a_1 (t-value)
ΔT_{eff}	T_{eff}	-1.82	1.82
ΔT_{eff}	$[\text{Fe}/\text{H}]$	0.29	1.24
$\Delta [\text{Fe}/\text{H}]$	T_{eff}	0.40	-0.40
$\Delta [\text{Fe}/\text{H}]$	$[\text{Fe}/\text{H}]$	1.03	4.28

We analysed the trends between the residuals and the observed atmospheric parameters by running linear regressions (see Figure 6). Table 4 shows that the only coefficient having a meaningful t-value (i.e., higher than 2) is the angular coefficient of the $\Delta[\text{Fe}/\text{H}]$ vs $[\text{Fe}/\text{H}]$ regression. Considering our preferred simple calibration based on MA15, our residuals in $[\text{Fe}/\text{H}]$ reach at most 0.25 dex and, taking into account these numbers, we chose to improve our $[\text{Fe}/\text{H}]$ determinations only by applying a simple linear correction to our $[\text{Fe}/\text{H}]_{\text{PCA}}$ values, thus arriving at the corrected $[\text{Fe}/\text{H}]_{\text{PCA}}^{\text{corr}}$ values (Equation 5):

$$[\text{Fe}/\text{H}]_{\text{PCA}}^{\text{corr}} = \frac{[\text{Fe}/\text{H}]_{\text{PCA}}}{0.6741(\pm 0.0762)}. \quad (5)$$

We replotted the residuals with the new $[\text{Fe}/\text{H}]_{\text{PCA}}^{\text{corr}}$ values (see Figure 7) and the trend with $[\text{Fe}/\text{H}]$ was completely removed along with a slightly decrease of the trend with T_{eff} . We found -1.5 and 0 t-values for the angular coefficients of T_{eff} and $[\text{Fe}/\text{H}]$, respectively. The PCA method is heavily based on the line index strengths, and these are at least partially degenerate between the T_{eff} and $[\text{Fe}/\text{H}]$ values, so a degree of correlation between the results of these two parameters is expected. It is probably impossible, within the limitations of the technique we employ, to completely eliminate these

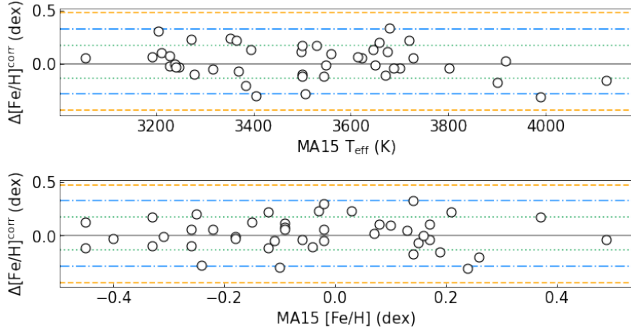


Figure 7. Corrected metallicity residuals versus observed T_{eff} and $[\text{Fe}/\text{H}]$ in the upper and bottom panels, respectively. We completely removed the trend with $[\text{Fe}/\text{H}]$ and slightly decreased the trend with T_{eff} . The grey solid lines represent the zero, green dotted lines are $\pm 1\sigma$, blue dash-dotted lines are $\pm 2\sigma$ and orange dashed lines are $\pm 3\sigma$ of the distributions.

trends, and this result speaks clearly of the difficulties in deriving consistently both T_{eff} and $[\text{Fe}/\text{H}]$ for red dwarfs when both parameters are determined still very far from fundamental considerations (i.e., hypothesis free), unlike what is nowadays possible for FGK stars (e.g., Smiljanic et al. 2014). These values are, in our judgment, the best T_{eff} and $[\text{Fe}/\text{H}]$ determinations from the line index measurements coupled to the $J - H$ color.

6 ATMOSPHERIC PARAMETERS DETERMINATION

6.1 Final effective temperature and $[\text{Fe}/\text{H}]$ and associated errors

To properly explore the full uncertainty range in the EWs of the spectral indices, we performed 1000 Monte Carlo (MC) simulations assuming that the EWs errors follow Gaussian distributions ($J - H$ values were not simulated). Thus, each spectrum originated 1000 different spectra and, consequently, a distribution of atmospheric parameters from which the most probable value was located at the center of the distribution (see Figure 8). The final T_{eff} and $[\text{Fe}/\text{H}]$ values found for each spectrum, hereafter called $T_{\text{eff}}^{\text{PCA}}$ and $[\text{Fe}/\text{H}]^{\text{PCA}}$, are the medians of the distribution. The final uncertainties associated with the atmospheric parameters are the propagation of the residual errors of the calibrations and the standard deviations of the distributions, but $[\text{Fe}/\text{H}]^{\text{PCA}}$ has an extra term related to the uncertainty of the linear correction term (Equations 6 and 7).

$$\sigma_{T_{\text{eff}}^{\text{PCA}}} = \sqrt{81.26^2 + \sigma_{\text{dist}}^2} \quad (6)$$

$$\sigma_{[\text{Fe}/\text{H}]^{\text{PCA}}} = \sqrt{0.1147^2 + \sigma_{\text{dist}}^2 + 0.0762^2} \quad (7)$$

This approach to error estimation of the final atmospheric parameters is interesting because it takes into account the position of each spectrum (i.e., the measurements of the EWs of each spectral index) in the parameter space. What it does not take into account is the specific S/N ratio of a given spectrum, since we are considering only a mean value for each spectral index uncertainty. However, we think this simplified approach does not introduce any large uncertainty since the S/N distribution of the spectra of the calibrating stars is very similar to the overall distribution of S/N ratios.

We applied this procedure to the calibration stars in order

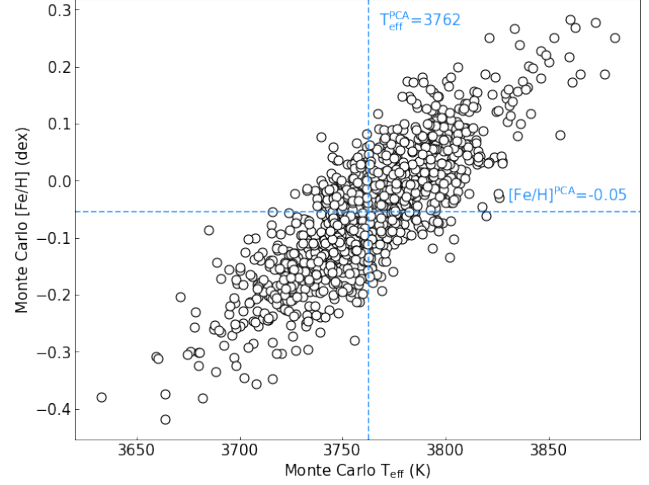


Figure 8. Distribution of the atmospheric parameters found for HIP 51007 (M1V). The dashed blue lines represent the median of each atmospheric parameter, i.e., 3763 K for $T_{\text{eff}}^{\text{PCA}}$ and -0.05 dex for $[\text{Fe}/\text{H}]^{\text{PCA}}$.

to verify the consistency of the atmospheric parameters obtained with the PCA calibrations using MC simulations. As shown in Figure 9, we satisfactorily recovered the atmospheric parameters values from Mann et al. (2015) and found a mean difference of 0 ± 64 K and 0.02 ± 0.15 dex and a median difference of -3 K and 0.01 dex for T_{eff} and $[\text{Fe}/\text{H}]$, respectively. Greater uncertainties for $[\text{Fe}/\text{H}]^{\text{PCA}}$ were expected considering that $[\text{Fe}/\text{H}]$ is difficult to derive due to its low sensitivity to the spectral indices, i.e., it is represented by lower PCs. Furthermore, we stress that, even though we removed all three indices corresponding to the Ca II triplet, chromospheric activity might still be affecting other spectral indices. This is unlikely since the two stronger lines of the Ca II triplet, $\lambda 8498$ ($i60$) and $\lambda 8662$ ($i105$), are the most opaque spectral features in our coverage (see Figure 2), excepting for the very cool types. Chromospheric fill-in in the triplet lines would have to be very strong to appear in other features, and only for the most active stars in our sample does the filling become appreciable. If spectral indices are affected by chromospheric activity, our results will only have a greater dispersion but this should not affect the accuracy – since the PCA technique minimizes the contributions of parameters that do not have a great impact on the total form of the spectrum. The residuals for both atmospheric parameters are shown in Figure 10 and we found a similar trend with the residuals previously discussed in Sect. 5.2. Values for the final atmospheric parameters of the calibration sample are given in Table 5.

We explored the correlation between Mann et al. (2015) atmospheric parameters, the uncertainties of the final atmospheric parameters delivered by our PCA calibration and the nominal S/N of the spectra and found a strong trend for $T_{\text{eff}}^{\text{PCA}}$ residuals. Figure 11 shows that cooler stars have lower S/N due to the exposure times of these objects (see Table 1), but even for cooler stars there is a decrease of the average uncertainties when we achieve higher S/N. On the other hand, $[\text{Fe}/\text{H}]$ values are better distributed between the PCA-based uncertainties and S/N, indicating that there are no systematic errors associated with the $[\text{Fe}/\text{H}]$ values themselves, i.e., higher metallicities do not necessarily have higher uncertainties.

We applied the same procedure to the 134 stars which are not part of the calibration sample (hereafter called “study sample”). For this case, all values outside the parameter space of the calibration

Table 5. Final atmospheric parameters for the calibration stars obtained by the PCA-based MC distributions. Column 1 lists the identifiers used for the stars. Columns 2 and 3 list the coordinates in J2000. Columns 4, 5 and 6 list $T_{\text{eff}}^{\text{MA15}}$ and $T_{\text{eff}}^{\text{PCA}}$ and uncertainties from this work, respectively. Columns 7, 8 and 9 list $[\text{Fe}/\text{H}]^{\text{MA15}}$ and $[\text{Fe}/\text{H}]^{\text{PCA}}$ and uncertainties from this work, respectively. Columns 10 and 11 list the calculated radial velocities and uncertainties. Column 12 lists nominal S/N of the spectra. Column 13 lists spectral types from MA15. $T_{\text{eff}}^{\text{MA15}}$ and $[\text{Fe}/\text{H}]^{\text{MA15}}$ uncertainties are 60 K and 0.08 dex, respectively, according to other authors.

Name	RA J2000	DEC J2000	$T_{\text{eff}}^{\text{MA15}}$ (K)	$T_{\text{eff}}^{\text{PCA}}$ (K)	$\sigma T_{\text{eff}}^{\text{PCA}}$ (K)	$[\text{Fe}/\text{H}]^{\text{MA15}}$ (dex)	$[\text{Fe}/\text{H}]^{\text{PCA}}$ (dex)	$\sigma[\text{Fe}/\text{H}]^{\text{PCA}}$ (dex)	RV (km/s)	σRV (km/s)	S/N	SpT ^{MA15}
HIP 5643	01:12:30.60	-16:59:56.30	3056±60	3174	128	-0.26±0.08	-0.3	0.29	31.18	1.04	134.70.80	M4.9
HIP 8768	01:52:49.10	-22:26:05.40	3900±60	3921	63	0.14±0.08	0.31	0.12	13.23	0.96	333.251	M0.2
HIP 12781	02:44:15.50	25:31:24.10	3405±60	3461	157	-0.10±0.08	0.21	0.36	39.22	1.18	80	M3.0
HIP 21556	04:37:41.80	-11:02:19.90	3671±61	3594	101	-0.04±0.08	0.07	0.18	-4.84	0.87	260	M2.0
HIP 21932	04:42:55.70	18:57:29.30	3680±60	3594	107	0.14±0.08	-0.19	0.25	17.83	0.64	130	M2.2
HIP 22762	04:53:49.90	-17:46:24.30	3506±60	3540	111	-0.24±0.08	0.04	0.2	-13.28	1.02	274	M2.1
HIP 23512	05:03:20.00	-17:22:24.70	3365±60	3307	161	-0.12±0.08	-0.33	0.39	16.86	2.15	100	M3.2
HIP 25878	05:31:27.30	-03:40:38.00	3801±60	3755	147	0.49±0.08	0.54	0.58	11.01	0.54	220.595	M1.5
HIP 36208	07:27:24.40	05:13:32.83	3317±60	3250	200	-0.11±0.08	-0.05	0.43	14.08	0.73	210	M3.8
HIP 40501	08:16:07.90	01:18:09.20	3500±60	3566	116	-0.12±0.08	-0.01	0.24	75.43	0.93	190	M2.2
HIP 49986	10:12:17.60	-03:44:44.30	3623±60	3640	107	0.13±0.08	0.08	0.22	20.61	0.95	180	M1.9
HIP 51007	10:25:10.80	-10:13:43.20	3700±60	3776	62	-0.02±0.08	0.02	0.13	21.06	1.2	199.233	M1.5
HIP 51317	10:28:55.50	00:50:27.60	3548±60	3540	113	-0.18±0.08	-0.17	0.23	20.65	0.8	170	M2.2
HIP 53020	10:50:52.00	06:48:29.20	3238±60	3211	214	0.16±0.08	0.16	0.44	1.41	2.75	150	M3.9
HIP 57548	11:47:44.30	00:48:16.40	3192±60	3170	225	-0.02±0.08	-0.07	0.45	-33.02	1.12	190	M4.3
GJ 3707	12:10:05.60	-15:04:16.90	3385±60	3232	207	0.26±0.08	0.44	0.26	78.64	0.77	218	M3.8
HIP 62687	12:50:43.50	-00:46:05.20	3989±60	4015	103	0.24±0.08	0.54	0.27	0.08	1.53	305	K7.9
GJ 512a	13:28:21.00	-02:21:37.10	3498±60	3509	129	0.08±0.08	-0.03	0.27	-38.74	1.92	283	M3.1
HIP 65859	13:29:59.70	10:22:37.70	3727±61	3721	91	-0.09±0.08	-0.15	0.19	30.45	1.24	160	M1.1
HIP 67155	13:45:43.70	14:53:29.40	3649±60	3565	154	-0.31±0.08	-0.3	0.54	39.34	1.29	190	M1.4
HIP 71253	14:34:16.80	-12:31:10.40	3211±60	3201	105	0.17±0.08	0.11	0.18	1.55	0.71	70.233.130.180	M4.0
HIP 74995	15:19:26.80	-07:43:20.10	3395±60	3446	125	-0.15±0.08	-0.31	0.29	5.06	1.05	180	M3.2
HIP 80824	16:30:18.00	-12:39:45.30	3272±60	3354	133	-0.03±0.08	-0.25	0.2	-21.91	0.87	437	M3.6
HIP 82809	16:55:25.20	-08:19:21.30	3279±60	3318	157	-0.26±0.08	-0.16	0.26	11.11	1.56	232	M3.2
GJ 1207	16:57:05.70	-04:20:56.30	3229±60	3316	163	-0.09±0.08	-0.17	0.33	-3.16	1.29	232	M4.1
HIP 85295	17:25:45.20	02:06:41.10	4124±60	4034	96	0.19±0.08	0.35	0.21	-26.64	2.77	180	K7.4
HIP 85665	17:30:22.70	05:32:54.60	3675±60	3761	92	-0.09±0.08	-0.22	0.2	-15.87	1.88	150	M0.5
HIP 86287	17:37:53.30	18:35:30.10	3657±60	3672	91	-0.25±0.08	-0.45	0.19	-12.53	1.62	140	M1.2
HIP 87937	17:57:48.40	04:41:36.10	3228±60	3275	118	-0.40±0.08	-0.36	0.2	-11.21	0.47	520.18	M4.2
HIP 88574	18:05:07.50	-03:01:52.70	3614±60	3670	92	-0.22±0.08	-0.29	0.2	32.08	1.1	160	M1.3
HIP 92403	18:49:49.30	-23:50:10.40	3240±60	3313	212	-0.18±0.08	-0.17	0.55	-11.94	1.07	180	M4.1
HIP 93873	19:07:05.50	20:53:16.90	3500±60	3452	130	-0.33±0.08	-0.21	0.32	32.55	1.42	218	M2.1
HIP 93899	19:07:13.20	20:52:37.20	3494±62	3415	152	-0.35±0.08	-0.49	0.5	34.44	2.42	90	M2.1
HIP 94761	19:16:55.20	05:10:08.00	3558±60	3528	125	0.10±0.08	0.01	0.26	34.67	0.73	200	M2.6
HIP 103039	20:52:33.00	-16:58:29.00	3205±60	3166	149	-0.02±0.08	-0.33	0.38	15.87	1.17	130.8	M4.0
HIP 104432	21:09:17.40	-13:18:09.00	3545±60	3584	65	-0.45±0.08	-0.39	0.14	-6.16	1.29	223.139	M1.4
HIP 109388	22:09:40.30	-04:38:26.60	3530±60	3443	106	0.37±0.08	0.2	0.18	-14.22	0.6	294.17	M3.1
HIP 111571	22:36:09.60	-00:50:29.70	3916±61	3843	90	0.07±0.08	0.04	0.18	8.07	1.89	250	M0.6
HIP 113020	22:53:16.70	-14:15:49.30	3247±60	3268	156	0.17±0.08	0.22	0.36	0.02	0.61	170.15	M3.7
HIP 113296	22:56:34.80	16:33:12.30	3720±60	3799	93	0.21±0.08	-0.03	0.2	-28.81	1.17	110	M1.5
HIP 114046	23:05:52.00	-35:51:11.00	3688±86	3630	182	-0.06±0.08	-0.05	0.7	24.04	1.48	200	M1.1
GJ 896a	23:31:52.10	19:56:14.10	3353±60	3341	198	0.03±0.08	-0.2	0.6	0.89	2.39	102	M3.8
HIP 117473	23:49:12.50	02:24:04.40	3646±60	3576	90	-0.45±0.08	-0.58	0.18	-71.04	1.21	150	M1.4

sample are extrapolating the calibrations and can not provide trustful values, yet slight extrapolations outside the parameter space of the calibrating stars should not introduce any large errors.

6.2 Comparison with literature values

We compare our final atmospheric parameters with a variety of published studies employing photometric and spectroscopic determinations for a wider appraisal of the accuracy and precision of our approach. Casagrande et al. (2008) (hereafter, CA08) exploits the flux ratio in different optical-infrared bands as a sensitive indicator of atmospheric parameters⁵; Rojas-Ayala et al. (2012) (hereafter, RA12) estimates $[\text{Fe}/\text{H}]$ from Na I, Ca I, and H2O-K2 measurements and used the H2O-K2 index as an indicator of T_{eff} ; Neves et al. (2014) (hereafter, NE14) estimations were based on the measurement of pseudo equivalent widths of features in the 530-690 nm range of HARPS spectra; Newton et al. (2015) (hereafter, NW15)

T_{eff} are based on EWs of H-band spectral features and $[\text{Fe}/\text{H}]$ are derived following Mann et al. 2013a calibrations ($[\text{Fe}/\text{H}]_1$); López-Valdivia et al. (2019) (hereafter, LV19) uses high-resolution line-depths measurements in the H-band from Grating Infrared Spectrometer (IGRINS) spectra to estimate T_{eff} ; Kuznetsov et al. (2019) (hereafter, KU19) determines atmospheric parameters by fitting the observed HARPS spectra with a grid of BT-Settl stellar atmosphere models; Hejazi et al. (2020) (hereafter, HE20) uses the BT-Settl model atmospheres to derive atmospheric parameters of low-to medium-resolution spectra; Antoniadis-Karnavas et al. (2020) (hereafter, AK20) uses a machine learning tool (ODUSSEAS) to derive atmospheric parameters based on the measurement of the pseudo equivalent widths for more than 4000 stellar absorption lines. The comparisons are shown in Figures 12 and 13 and the following discussion is limited to stars lying within the parameter space of our calibrations.

Regarding T_{eff} , we notice that our values have a systematic overestimation of 186 ± 255 K, 349 ± 206 K and 219 ± 271 K compared to CA08, NE14 and AK20, respectively. NE14 and AK20 estimations were calibrated following CA08 values (explaining their mutual consistency) which uses black-body approximations for M dwarfs in the infrared. Depression of the local pseudo continuum by molecular line blanketing may have led to an underestimation of the

⁵ Quoted from Casagrande et al. 2008: “The model atmospheres are given for the total heavy elements, but for low values of alpha-enhancement, the difference between the two is negligible, particularly since metallicity measurements in M dwarfs are still uncertain.”.

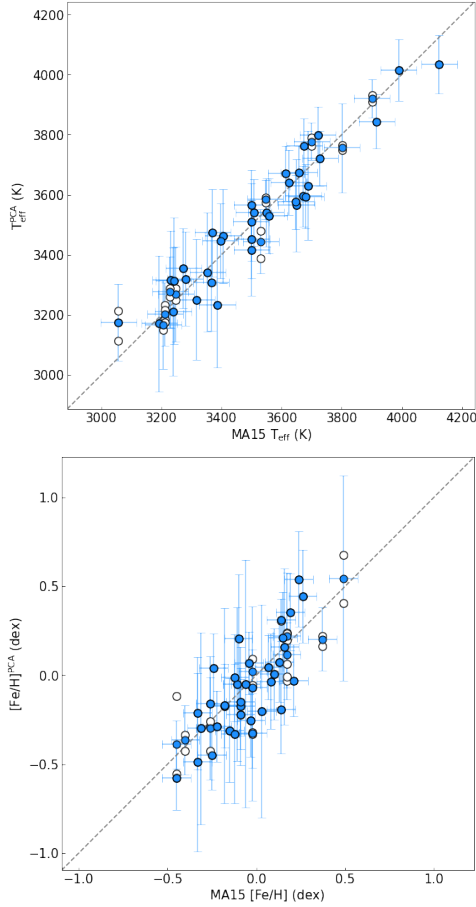


Figure 9. Comparison between the atmospheric parameters from MA15 and the final values from the PCA-based calibrations using MC simulations. The dashed grey lines represent equality. The white circles are the atmospheric parameters found for each spectrum and the blue ones are the final values (weighted mean) representing each star. We have 44 calibration stars for which 10 have more than one spectrum, giving a total of 57 spectra. We found mean differences (related to the blue dots) of 0 ± 64 K and 0.02 ± 0.15 dex for T_{eff} and $[\text{Fe}/\text{H}]$, respectively.

flux and hence an underestimation of T_{eff} . We found an excellent agreement of 11 ± 133 K and 47 ± 199 K for T_{eff} between our values and NW15 and LV19, respectively, both based on H-band spectral features, and -40 ± 227 K with RA12 and 12 ± 140 K with HE20. Lastly, we found a difference of 84 ± 309 K with KU19, showing a significant zero-point discrepancy but contained by a large dispersion. This exceptional agreement with NW15 values was expected since they based their work on interferometric measurements in common with MA15. We recall that the mean and median $T_{\text{eff}}^{\text{PCA}}$ uncertainties are 132 K and 105 K, respectively, for the study sample. From Figure 12 it is noteworthy that, even in the middle of the parameter range, T_{eff} offsets up to many hundreds of Kelvin are seen between published values, for example, between the barycenters of the CA08 and RA12 T_{eff} distributions. Our values tend to lie midrange in the distribution of published T_{eff} values.

Regarding $[\text{Fe}/\text{H}]$, we achieve good agreement with CA08, RA12, NE14, KU19 and HE20 with mean differences of 0.11 ± 0.24 dex, -0.11 ± 0.19 dex, 0.09 ± 0.26 dex, 0.07 ± 0.33 dex and -0.02 ± 0.25 dex, respectively, meaning that possibly not all scatter in these comparisons is due to our calibration (see also Table 6). Although NW15 $[\text{Fe}/\text{H}]_1$ is based on the same calibration used by Mann et al. 2015

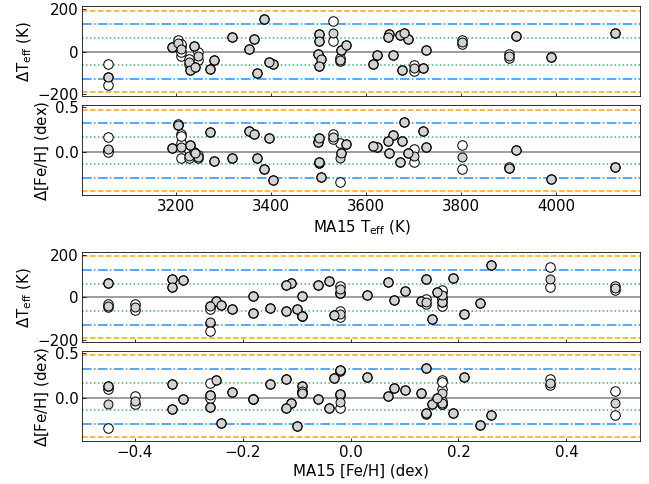


Figure 10. $T_{\text{eff}}^{\text{PCA}}$ and $[\text{Fe}/\text{H}]^{\text{PCA}}$ residuals versus T_{eff} and $[\text{Fe}/\text{H}]$ from MA15 in the upper and bottom panels, respectively. The white circles are the atmospheric parameters found for each spectrum and the grey ones are the final value (weighted mean) representing each star. We have 44 calibration stars for which 10 have more than one spectrum, giving a total of 57 spectra. We found mean differences (grey circles) of 0 ± 64 K and 0.02 ± 0.15 dex for T_{eff} and $[\text{Fe}/\text{H}]$, respectively. Our residuals reach at most 2σ approximately for both atmospheric parameters, the worst cases being the metal-richer and hotter K dwarf stars. The grey solid lines represent the zero, green dotted lines are $\pm 1\sigma$, blue dash-dotted lines are $\pm 2\sigma$ and orange dashed lines are $\pm 3\sigma$ of the distributions.

applicable to stars ranging $-1.04 < [\text{Fe}/\text{H}] < +0.56$ and spectral types from K7 to M5, we found one of the worst correlation of the comparisons with a mean difference of -0.16 ± 0.38 dex between theirs and our calibrated values. We found a weak correlation of 0.17 ± 0.25 with AK20, but we note that there are only 6 stars in common with our sample. We recall that the mean and median $[\text{Fe}/\text{H}]^{\text{PCA}}$ uncertainties are 0.28 dex and 0.23 dex, respectively, for the study sample. From Figure 13 we see that agreement for published $[\text{Fe}/\text{H}]$ is much better than for T_{eff} , and again our determinations lie midrange. Values for the final atmospheric parameters of 134 stars of the study sample are given in Table A3.

6.3 Appraisal of discrepancies between different sources

We next perform a more detailed overall comparison between the atmospheric parameters from different works: the results are shown in Table 6. This comparison considers analyses employing very different methods and heterogeneous sources of data. Intercomparisons comprising less than 10 stars are not statistically significant and will not be pursued. We begin by comparing T_{eff} values. Concerning our own determinations, it is apparent that intercomparisons involving our values tend to have large dispersions, though not exclusively. Important offsets are seen between our work and CA08 and NE14, even though contained within the large dispersions: our values are hotter in both cases. Large offsets are also seen when comparing CA08 to all authors but NE14 and AK20, as expected, since the latter's T_{eff} determinations were made consistent to the former's. Particularly significant are the discrepancies between the values of CA08-NE14 and those of RA12, NW15 and HE20, as the offsets clearly surpass the observed dispersions by large margins. The determinations of MA15, RA12, NW15 and LV19 are mutually consistent. Besides those that involve the values of this work, very large disper-

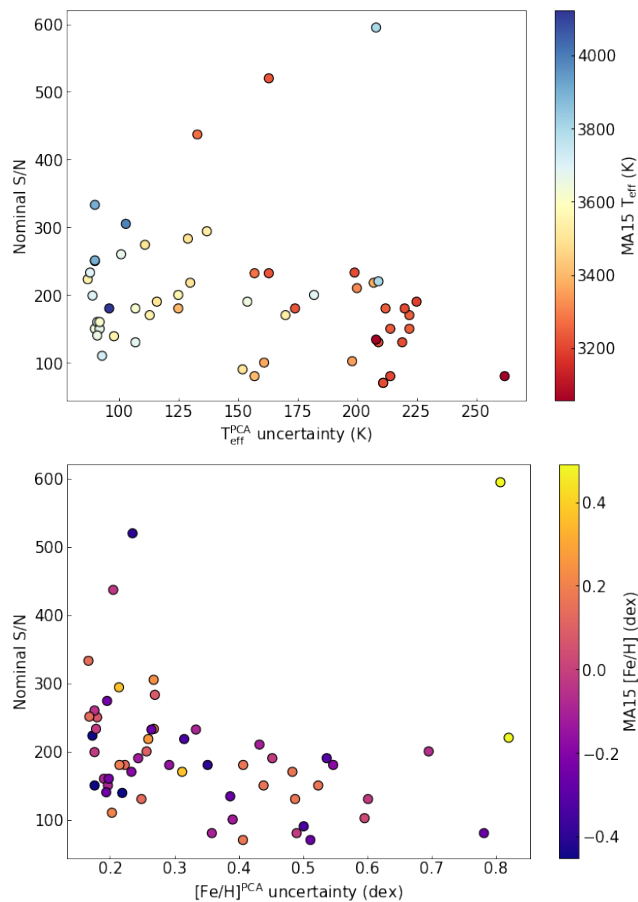


Figure 11. Correlation between the atmospheric parameters of MA15 and our $T_{\text{eff}}^{\text{PCA}}$ and $[\text{Fe}/\text{H}]^{\text{PCA}}$ values, with their respective uncertainties and nominal S/N on top and bottom panels, respectively, for 57 spectra of 44 calibration stars. The hot outlier on the top panel with uncertainty around 210 K is the spectrum of HIP 25878 (M1.5Ve) and this difference might be due to its extremely high S/N of 600 maybe introducing difficulties in applying the same index system based on lower S/N spectra.

sions are observed in the comparisons RA12/NE14, RA12/LV19, NE14/LV19, CA08/KU19, RA12/KU19, LV19/KU, CA08/HE20, MA15/HE20, NW15/HE20, LV19/HE20 and KU19/HE20 though not always associated with large offsets.

Intercomparisons involving $[\text{Fe}/\text{H}]$ determinations fare much better. Again, the largest dispersions are found when comparing our own values with those of other works, but the offsets are well contained by the dispersions. The largest statistically significant offsets in $[\text{Fe}/\text{H}]$ are seen between CA08/MA15, CA08/KU19, CA08/HE20 and NW15/HE20, the first one largely surpassing the dispersion. All other comparisons show good accord, and the dispersions are generally low, with some exceptions. The fact that some $[\text{Fe}/\text{H}]$ comparisons between sources with more precise determinations than our own show dispersions in the >0.10 dex range seems to justify our previous assertion that not all scatter seen in Figure 13 is due to our method.

Our atmospheric parameters are overall quite accurate but not very precise. Nonetheless, they are competitive with estimations that make use of high-resolution spectroscopy. We find a median difference of 75 ± 273 K and 0.02 ± 0.31 dex for T_{eff} and $[\text{Fe}/\text{H}]$, respectively. Lastly, considering the significant number of stars in

common between previously published studies, and the fact that most stars in common between this work and other authors' belong to the calibration sample itself (i.e., stars in common with Mann et al. 2015), it is noteworthy that here we present determinations of atmospheric parameters for a large number of M dwarfs for which previously such data were lacking.

6.4 M Dwarf Metallicity Distribution Function

Measuring the $[\text{Fe}/\text{H}]$ distribution of stars in the Milky Way disk is a fundamental tool of the study of its chemo-dynamical evolution. Cool dwarf stars from spectral types FGKM preserve in their atmospheres, with high fidelity, the chemical composition of their natal interstellar clouds. Moreover, GK dwarfs have lifetimes comparable to the age of the Galaxy, while lifetimes of M dwarfs vastly surpass the Galactic age: these stars thus provide an uninterrupted fossil record of chemical evolution. These chemical footprints are crucial constraints to the star formation history of the Galactic disk as well as its variation in time and space. Such data track the evolution of relevant physical processes such as kinematics, the structure and speed of enrichment, the mass function, the frequency and yields of core collapse and SNIa supernovae, the infall and outflow of gas, and the merging and accretion history. Spectroscopically derived metallicity distribution functions (MDF hereafter) of $[\text{Fe}/\text{H}]$ abundances have been extensively studied for the more massive FGK stars but data on the $[\text{Fe}/\text{H}]$ distribution for M dwarfs is much more scarce owing to the difficulty of volume-sampling these objects to appropriate depths. We thought it worthwhile to compare the $[\text{Fe}/\text{H}]$ distribution resulting from our M dwarf data from the immediate solar neighbourhood to the existing record for FGK dwarfs. We need to keep in mind that even in the immediate neighborhood incompleteness for magnitude-limited sampling of M dwarfs remains very high, particularly for the later types. Winters et al. (2015) find that the identification of M dwarf systems already loses completeness at distances not much farther than 5 pc.

The local disk MDF has been examined both by photometric determinations of $[\text{Fe}/\text{H}]$ (Rocha-Pinto & Maciel 1998, Nordström et al. 2004, Casagrande et al. 2011) and by spectroscopic $[\text{Fe}/\text{H}]$ estimations based on spectra with a wide range of spectral resolutions (Luck & Heiter 2005, 2006, 2007; Katz et al. 2011; Siebert et al. 2011 Schlesinger et al. 2012). From the many excellent resources available in the literature we chose to compare the $[\text{Fe}/\text{H}]$ distribution of our M dwarf sample to the statistically large RAVE survey (Boeche et al. 2013) by means of the $[\text{Fe}/\text{H}]$ determinations of their 4th Data Release (Kordopatis et al. 2013). The reasons for this choice are manifold. The RAVE survey sampled over 480,000 stars in the Milky Way at a spectral resolution of $R \sim 7,500$, for which distances were estimated and individual chemical abundances for six elements determined, of which only Fe concerns us here. RAVE is a magnitude-limited survey with constant integration time, and more distant stars have on average lower S/N spectra, not too dissimilar from our own observing strategy. The analysis of Boeche et al. (2013) limits the investigation to dwarf stars ($\log g > 3.8$ dex) with good quality RAVE spectra (i.e., good chemical abundances) and reliable distances, selecting only spectra with $S/N > 40$ in the $5250 \text{ K} < T_{\text{eff}} < 7000 \text{ K}$ range (i.e., early F to early K stars) with a resulting average uncertainty for $[\text{Fe}/\text{H}]$ of ~ 0.15 dex. Their selection yields 19,962 stars, most within 300 pc of the Galactic plane and in the galactocentric radius interval $7.6 \text{ kpc} < R_g < 8.3 \text{ kpc}$ (they assume $R_{\odot} = 8.0$ and R_g stands for guiding radius). Therefore, the RAVE survey concentrates on dwarf stars; its data possesses spectral resolution very similar to ours; its abundance

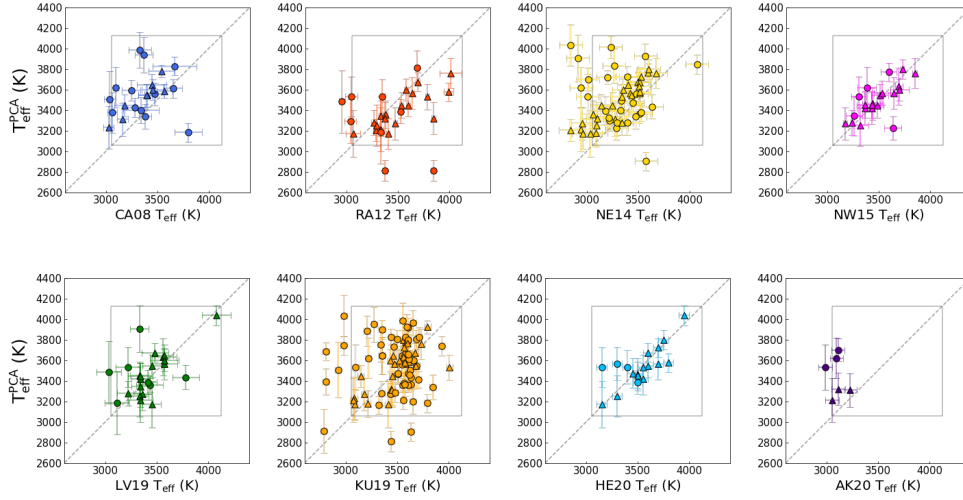


Figure 12. Comparison between our $T_{\text{eff}}^{\text{PCA}}$ for stars in common with other studies. The grey dashed lines represent equality and the boxes represent the limits of strict validity of our calibrations. The triangles represent the calibration stars and the circles represent sample stars – see text for details.

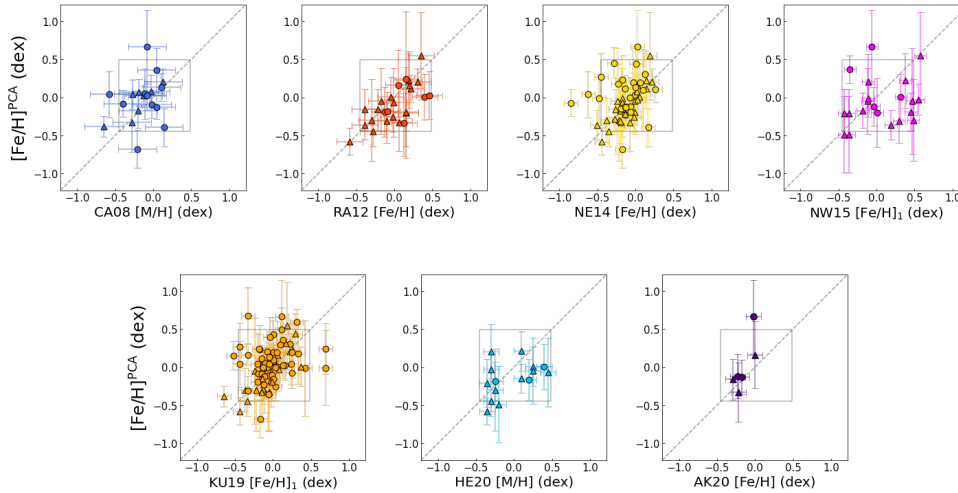


Figure 13. Comparison between our $[\text{Fe}/\text{H}]^{\text{PCA}}$ for stars in common with other studies. The grey dashed lines represent equality and the boxes represent the limits of strict validity of our calibrations. The triangles represent the calibration stars and the circles represent sample stars – see text for details.

errors are also comparable; and most of the RAVE sample is inside the scale height of the thin disk (0.3 kpc, as shown by the Figure 1 of Boeche et al. 2013), which is certainly the case for our sample of very nearby stars (see Sect. 7).

The $[\text{Fe}/\text{H}]$ distribution of the full sample of RAVE stars from Boeche et al. (2013) is shown in their Figure 2, and it has a well-defined peak at $[\text{Fe}/\text{H}] \sim -0.2$ dex. Particularly, their Figure 3 shows the distribution for those stars with $0.0 \text{ kpc} < |Z_{\text{max}}| < 0.4 \text{ kpc}$, where $|Z_{\text{max}}|$ stands for maximum excursion above the Galactic plane, and this distribution, from a sample fully dominated by thin disk stars, peaks at $[\text{Fe}/\text{H}]$ of -0.15 dex. Our own $[\text{Fe}/\text{H}]$ distribution, sampled to 0.2 dex to reflect external $[\text{Fe}/\text{H}]$ errors, and employing the atmospheric parameters derived from the PCA calibration even for the calibrating stars themselves, for the sake of consistency, is shown in Figure 14. It peaks at $[\text{Fe}/\text{H}] \sim -0.10$ dex. Our M dwarf MDF shows, thus, good agreement with that of FGK stars of the

local thin disk, within the uncertainties, and we conclude that the MDFs of FGKM stars in the local thin disk are consistent between these spectral types.

7 DYNAMIC CONFIGURATION IN THE GALACTIC STRUCTURES

Figure 15 shows the distribution of the M dwarfs in diagrams frequently used to determine the membership of the stars in the major Galactic substructures. These are the Lindblad and Toomre diagrams, and the eccentricity vs. Galactic radius (R_{Gal}). The Gaia nearby (distances within 100 pc) random data, represented by the gray dots, was plotted as background to facilitate the visualisation of the M dwarfs with respect to a representative reference in the solar surrounding. As expected, most of the stars remain within the areas corresponding to the thin and thick discs (e.g. Helmi &

Table 6. Mean differences of effective temperature and metallicity between our work and other authors. The right diagonal contains the number of stars in common between authors and the left diagonal contains the mean differences and standard deviations for the atmospheric parameters in K and dex. Differences are calculated in the following way: values of the parameters from the authors listed in the top row minus those values from the authors listed in the leftmost column. Comparisons containing 10 stars or less in common between authors should be considered with caution. See text for more details.

Ref.	Costa-Almeida	CA08	RA12	NE14	MA15	NW15	LV19	KU19	HE20	AK20
Costa-Almeida		22	27	52	44 ^a	21	23	81	18	6
CA08	186±255 0.11±0.24		3	14	19	3	10	81	10	3
RA12	-40±227 -0.11±0.19	-354±50 -0.20±0.02		26	62	26	50	19	0	7
NE14	210±278 0.09±0.26	12±70 -0.08±0.06	231±209 0.05±0.11		38	15	20	61	0	30
MA15	0±66 ^a 0.02±0.15 ^a	-143±102 -0.15±0.06	36±124 -0.04±0.09	-174±119 -0.07±0.09		36	53	55	56	9
NW15	11±133 -0.16±0.38	-274±130 -0.02±0.00	-27±102 -0.01±0.09	-161±169 -0.05±0.14	16±76 0.02±0.08		32	16	87	8
LV19	47±199	-142±140	-19±244	-233±331	11±118	9±111		27	49	3
KU19	84±309 0.07±0.33	-74±225 -0.21±0.19	92±230 0.00±0.12	-142±150 -0.06±0.07	42±164 0.00±0.12	-28±146 -0.13±0.19	21±288		32	20
HE20	12±140 -0.02±0.25	286±263 -0.23±0.32	-	-	97±332 0.05±0.56	-104±227 0.20±0.65	31±346	224±276 0.11±0.61		1
AK20	349±206 0.17±0.25	-19±36 -0.08±0.02	248±243 0.12±0.11	-12±101 0.04±0.06	168±51 0.11±0.06	132±101 0.10±0.14	235±149	190±101 0.08±0.05	226±0 0.61±0	

^a Calibration sample

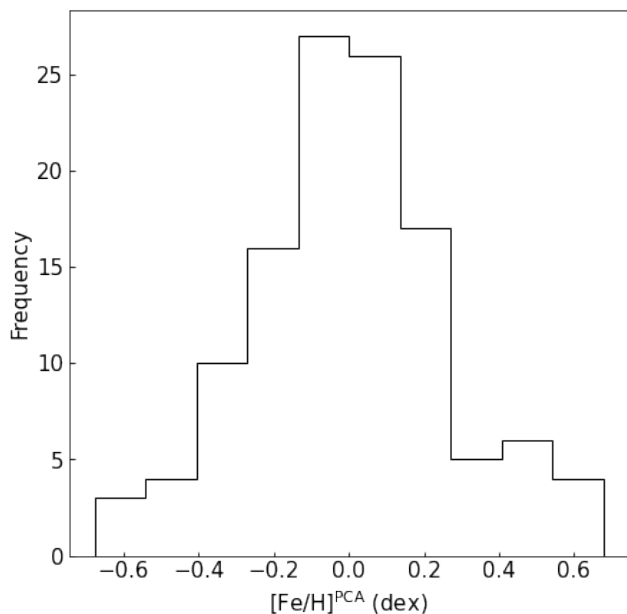


Figure 14. The raw $[\text{Fe}/\text{H}]$ distribution of all $[\text{Fe}/\text{H}]_{\text{PCA}}$ determinations derived in this study, out to 25 pc, binned to 0.2 dex intervals.

de Zeeuw 2000; Gallart et al. 2019; Massari et al. 2019, among many others). In the Toomre diagram this area is enclosed by the dashed line, the radius of which was set to $V_{\phi \text{ total}} = 180 \text{ km s}^{-1}$. The $V_{\phi \text{ total}}$ quantity is frequently defined as the velocity module that separates prograde and retrograde movements; for example, Bonaca et al. (2017) adopts 220 km s^{-1} . However, it is important to keep in mind that a fixed figure is just a representative value to separate the halo and the discs, the velocity distributions of which may naturally overlap.

HIP 24186 is the only star to stand clearly outside of the areas

covered by the disc stars in every diagram. This object is the well-known high-velocity Kapteyn's star. According to our modelling it has a low orbital energy, a slightly retrograde movement $V \approx -50 \text{ km s}^{-1}$, and a quite eccentric orbit ~ 0.75 . It is a moderately metal-rich star for such kinematics, in the range $[\text{Fe}/\text{H}] \sim -0.60$ dex to -0.90 dex (e.g., Hojjatpanah et al. 2019; Arentsen et al. 2019). Metal-rich stars with low Z distances and retrograde movements have been identified as members of the in-situ formed halo, which has a wide $[\text{Fe}/\text{H}]$ distribution that ranges from -2 dex to the solar value according to the analysis of Bonaca et al. (2017). There, the authors discuss that radial migration, promoted by the accretion of intergalactic medium and satellite galaxies, is a mechanism that can possibly explain in-situ halo stars well dispersed around $V = 0 \text{ km s}^{-1}$ in the Toomre diagram. In such a case, HIP 24186 should be older than the rest of M dwarfs in the current sample to be consistent with a metal-rich halo formed prior to the thin disc (Ma et al. 2017). Still, although it is rare, a few in-situ halo stars may invade the area covered by the discs as shown by the simulations presented in Bonaca et al. (2017).

Metal-rich stars with halo kinematics can be also members of the so called "splashed disc" structure, the dynamics of which is interpreted as the consequence of the accretion events. According to El-Badry et al. (2016), some stars can be formed during gas outflows driven by stellar feedback, thus they may have quite eccentric initial orbits. In such a case, HIP 24186 could be dated contemporary to the merging event that promoted its formation, hence it should be somewhat younger than in-situ halo scattered stars.

Therefore, our $[\text{Fe}/\text{H}]$ data plus kinematics strongly suggest that our sample is fully dominated by thin and thick disk stars, as expected.

8 CONCLUSIONS

We present T_{eff} and $[\text{Fe}/\text{H}]$ determinations for 178 M dwarfs located within 25 parsecs of the Sun, by means of a new system of 147 spectral indices measured in the $\lambda\lambda 8390\text{-}8834 \text{ \AA}$ range and coupled

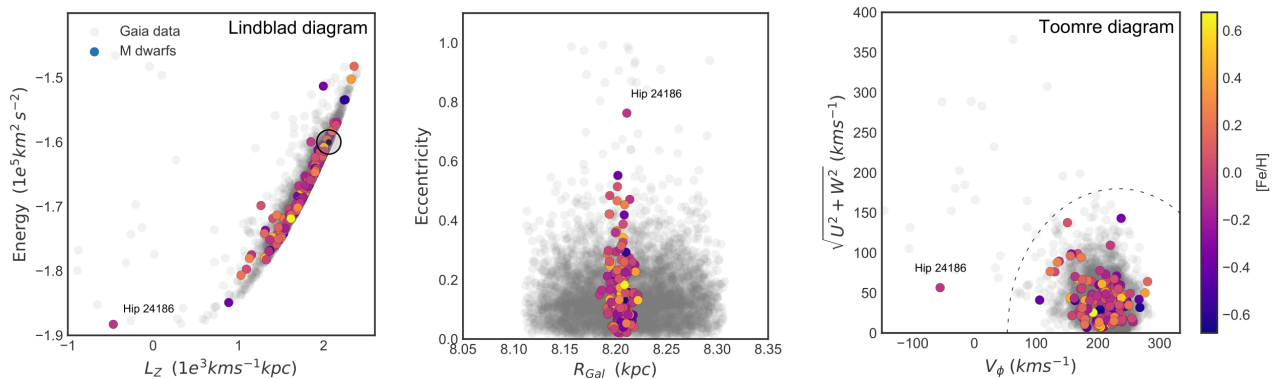


Figure 15. M dwarfs and Gaia random stars within 10 pc in the Lindblad diagram (left panel), in the eccentricity vs. R_{Gal} diagram (mid panel), and in the Toomre diagram (right panel). Our red dwarf data are color coded according to the bar in the right panel, whereas the Gaia random stars are shown in gray. In the left panel, the position of the Sun is indicated with the \odot symbol. In the right panel, the dashed line corresponds to $V_{\phi, \text{total}} = 180 \text{ km s}^{-1}$ with respect to the local standard of rest.

to the $J - H$ color. The indices are defined in moderate resolution ($R \sim 11,000$) and moderately high S/N spectra (≥ 100), obtained at the coude spectrograph of the 1.60 m Perkin-Elmer telescope of Observatório do Pico dos Dias, Brazil. A PCA regression applied to the indices and $J - H$ color was calibrated for 44 M dwarfs with well determined parameters (Mann et al. 2015). The calibration achieved, respectively, an internal precision of 81 K and 0.12 dex for T_{eff} and [Fe/H]. Total median uncertainties estimated from Monte Carlo propagation of errors are, respectively, 105 K and 0.23 dex for T_{eff} and [Fe/H]. Radial velocities with mean internal precision of 1.4 km/s are also presented, for many objects for the first time.

Our conclusions are as follows:

- the comparison of our atmospheric parameters with others available in the literature, employing a wide variety of both photometric and spectroscopic methods, reveals considerable discrepancies between published works, both in zero-point and scale, up to a few hundred Kelvin in the worst cases. The median differences of $75 \pm 273 \text{ K}$ and $0.02 \pm 0.31 \text{ dex}$ for T_{eff} and [Fe/H], respectively. Our values are thus accurate but present lower precision when compared to those of most authors;
- the PCA-calibrated spectral indices constitute a model-free, rather competitive technique able to retrieve atmospheric parameters with good accuracy and reasonable precision, well suited to the extensive databases of M dwarf spectra in the far red;
- our raw, uncorrected metallicity distribution function of [Fe/H] for nearby M dwarfs shows a peak at [Fe/H] $\sim -0.10 \text{ dex}$, in very good agreement with the RAVE (Boeche et al. 2013) metallicity distribution function for 19,962 FGK dwarf stars, most of them contained within $0.0 \text{ kpc} < |Z_{\text{max}}| < 0.4 \text{ kpc}$, corresponding to the local thin disk. The MDFs for FGKM spectral types appear thus to be consistent to one another;
- investigation of the Galactic orbits of the sample stars shows that the whole sample can be safely ascribed to the thin and thick disk, the only notable exception being the well-know metal-poor red dwarf Kapteyn’s star. Our modelling strongly suggests the complete dominance of thick and thin disk stars in our sample.

Current and future projects focusing in M dwarfs (such as CARMENES, Reiners et al. 2018) can benefit from our spectral index approach which is able to derive accurate T_{eff} and [Fe/H] for large samples of M dwarfs employing spectra of relatively modest quality. Gaia Data Release 3 Catalogue (expected to the first half of

2022) will contain spectra of millions of stars – spectra which will have a similar resolution to the ones used in this work. Thus, our method can be easily applied to the millions of M dwarfs that Gaia contemplates. This represents an unique opportunity to globally characterize the most abundant objects in the Galaxy.

DATA AVAILABILITY

The data underlying this article will be shared on reasonable request to the corresponding author.

ACKNOWLEDGEMENTS

E.C.A. acknowledges CNPq/Brazil and CAPES/Brazil scholarships. G.F.P.M. acknowledges grant 474972/2009-7 from CNPq/Brazil. M.L.U.M. acknowledges CAPES/Brazil and FAPERJ scholarships. D.L.O. acknowledges a CAPES/Brazil scholarship and a FAPESP 2016/20667-8 grant. R.E.G. acknowledges scholarships from CAPES/Brazil and ESO, and the support by the National Science Centre, Poland, through project 2018/31/B/ST9/01469. We thank H. J. Rocha-Pinto for helpful discussions. We thank the referee, Dr. Eduardo Martin, for criticism and suggestions that considerably improved the manuscript. We thank the staff of OPD/LNA for considerable support in the many observing runs carried out during this project. Use was made of the Simbad database, operated at the CDS, Strasbourg, France, and of NASA’s Astrophysics Data System Bibliographic Services. This publication makes use of data products from the Two Micron All Sky Survey, which is a joint project of the University of Massachusetts and the Infrared Processing and Analysis Center/California Institute of Technology, funded by the National Aeronautics and Space Administration and the National Science Foundation. This work presents results from the European Space Agency (ESA) space mission Gaia. The Gaia data are being processed by the Gaia Data Processing and Analysis Consortium (DPAC). Funding for the DPAC is provided by national institutions, in particular the institutions participating in the Gaia MultiLateral Agreement (MLA). The Gaia mission website is <https://www.cosmos.esa.int/gaia>. The Gaia archive website is <https://archives.esac.esa.int/gaia>. This research made

use of Astropy⁶, a community-developed core Python package for Astronomy (Astropy Collaboration et al. 2013, 2018).

REFERENCES

- Antoniadis-Karnavas A., Sousa S. G., Delgado-Mena E., Santos N. C., Teixeira G. D. C., Neves V., 2020, *A&A*, **636**, A9
- Arentsen A., et al., 2019, *A&A*, **627**, A138
- Astropy Collaboration et al., 2013, *A&A*, **558**, A33
- Astropy Collaboration et al., 2018, *AJ*, **156**, 123
- Boeche C., et al., 2013, *A&A*, **553**, A19
- Bonaca A., Conroy C., Wetzel A., Hopkins P. F., Kereš D., 2017, *ApJ*, **845**, 101
- Bonfils X., Delfosse X., Udry S., Santos N. C., Forveille T., Ségransan D., 2005, *A&A*, **442**, 635
- Bonfils X., et al., 2013, *A&A*, **549**, A109
- Boyajian T. S., et al., 2012, *ApJ*, **757**, 112
- Casagrande L., Flynn C., Bessell M., 2008, *MNRAS*, **389**, 585
- Casagrande L., Schönrich R., Asplund M., Cassisi S., Ramírez I., Meléndez J., Bensby T., Feltzing S., 2011, *A&A*, **530**, A138
- Czesla S., Schröter S., Schneider C. P., Huber K. F., Pfeifer F., Andreasen D. T., Zechmeister M., 2019, PyA: Python astronomy-related packages (ascl:1906.010)
- Dressing C. D., Charbonneau D., 2013, *ApJ*, **767**, 95
- El-Badry K., Wetzel A., Geha M., Hopkins P. F., Kereš D., Chan T. K., Faucher-Giguère C.-A., 2016, *ApJ*, **820**, 131
- Gaia Collaboration et al., 2021, *A&A*, **649**, A9
- Gallart C., Bernard E. J., Brook C. B., Ruiz-Lara T., Cassisi S., Hill V., Monelli M., 2019, *Nature Astronomy*, **3**, 932
- Ghezzi L., et al., 2014, *AJ*, **148**, 105
- Ghezzi L., Montet B. T., Johnson J. A., 2018, *ApJ*, **860**, 109
- Giribaldi R. E., Porto de Mello G. F., Lorenzo-Oliveira D., Amôres E. B., Ubaldo-Melo M. L., 2019, arXiv e-prints, p. [arXiv:1907.00445](https://arxiv.org/abs/1907.00445)
- Hejazi N., Lépine S., Homeier D., Rich R. M., Shara M. M., 2020, *AJ*, **159**, 30
- Helmi A., de Zeeuw P. T., 2000, *MNRAS*, **319**, 657
- Hobson M. J., Jofré E., García L., Petrucci R., Gómez M., 2018, *Rev. Mex. Astron. Astrofis.*, **54**, 65
- Hojjatpanah S., et al., 2019, *A&A*, **629**, A80
- Jeffers S. V., et al., 2020, *Science*, **368**, 1477
- Katz D., Soubiran C., Cayrel R., Barbuy B., Friel E., Bienaymé O., Perrin M. N., 2011, *A&A*, **525**, A90
- Kirkpatrick J. D., et al., 2012, *ApJ*, **753**, 156
- Kordopatis G., et al., 2013, *AJ*, **146**, 134
- Kuznetsov M. K., del Burgo C., Pavlenko Y. V., Frith J., 2019, *ApJ*, **878**, 134
- Lindgren S., Heiter U., Seifahrt A., 2016, *A&A*, **586**, A100
- López-Valdivia R., et al., 2019, *ApJ*, **879**, 105
- Lorenzo-Oliveira D., Porto de Mello G. F., Dutra-Ferreira L., Ribas I., 2016, *A&A*, **595**, A11
- Luck R. E., Heiter U., 2005, *AJ*, **129**, 1063
- Luck R. E., Heiter U., 2006, *AJ*, **131**, 3069
- Luck R. E., Heiter U., 2007, *AJ*, **133**, 2464
- Ma X., Hopkins P. F., Wetzel A. R., Kirby E. N., Anglés-Alcázar D., Faucher-Giguère C.-A., Kereš D., Quataert E., 2017, *MNRAS*, **467**, 2430
- Mann A. W., Brewer J. M., Gaidos E., Lépine S., Hilton E. J., 2013a, *AJ*, **145**, 52
- Mann A. W., Gaidos E., Ansdell M., 2013b, *ApJ*, **779**, 188
- Mann A. W., Deacon N. R., Gaidos E., Ansdell M., Brewer J. M., Liu M. C., Magnier E. A., Aller K. M., 2014, *AJ*, **147**, 160
- Mann A. W., Feiden G. A., Gaidos E., Boyajian T., von Braun K., 2015, *ApJ*, **804**, 64
- Massari D., Koppelman H. H., Helmi A., 2019, *A&A*, **630**, L4
- Matheson T., Filippenko A. V., Ho L. C., Barth A. J., Leonard D. C., 2000, *AJ*, **120**, 1499
- McMillan P. J., 2017, *MNRAS*, **465**, 76
- Montes D., et al., 2018, *MNRAS*, **479**, 1332
- Neves V., et al., 2012, *A&A*, **538**, A25
- Neves V., Bonfils X., Santos N. C., Delfosse X., Forveille T., Allard F., Udry S., 2014, *A&A*, **568**, A121
- Newton E. R., Charbonneau D., Irwin J., Berta-Thompson Z. K., Rojas-Ayala B., Covey K., Lloyd J. P., 2014, *AJ*, **147**, 20
- Newton E. R., Charbonneau D., Irwin J., Mann A. W., 2015, *ApJ*, **800**, 85
- Nordström B., et al., 2004, *A&A*, **418**, 989
- Oh S., Price-Whelan A. M., Brewer J. M., Hogg D. W., Spergel D. N., Myles J., 2018, *ApJ*, **854**, 138
- Perryman M. A. C., et al., 1997, *A&A*, **500**, 501
- Rabus M., et al., 2019, *MNRAS*, **484**, 2674
- Reiners A., et al., 2018, *A&A*, **612**, A49
- Rocha-Pinto H. J., Maciel W. J., 1998, *A&A*, **339**, 791
- Rojas-Ayala B., Covey K. R., Muirhead P. S., Lloyd J. P., 2012, *ApJ*, **748**, 93
- Sahlmann J., et al., 2021, *MNRAS*, **500**, 5453
- Santos N. C., Israelian G., Mayor M., 2004, *A&A*, **415**, 1153
- Schlesinger K. J., et al., 2012, *ApJ*, **761**, 160
- Schönrich R., Binney J., Dehnen W., 2010, *MNRAS*, **403**, 1829
- Ségransan D., Kervella P., Forveille T., Queloz D., 2003, *A&A*, **397**, L5
- Siebert A., et al., 2011, *AJ*, **141**, 187
- Smiljanic R., et al., 2014, *A&A*, **570**, A122
- Soubiran C., et al., 2018, *A&A*, **616**, A7
- Teske J. K., Ghezzi L., Cunha K., Smith V. V., Schuler S. C., Bergemann M., 2015, *ApJ*, **801**, L10
- Tuomi M., Jones H. R. A., Barnes J. R., Anglada-Escudé G., Jenkins J. S., 2014, *MNRAS*, **441**, 1545
- Tuomi M., et al., 2019, arXiv e-prints, p. [arXiv:1906.04644](https://arxiv.org/abs/1906.04644)
- Valenti J. A., Fischer D. A., 2005, *ApJS*, **159**, 141
- Winters J. G., et al., 2015, *AJ*, **149**, 5
- von Braun K., et al., 2014, *MNRAS*, **438**, 2413

APPENDIX A: DATA

This paper has been typeset from a $\text{\TeX}/\text{\LaTeX}$ file prepared by the author.

⁶ <http://www.astropy.org>

Table A1. Spectral indices defined from 8390.170 to 8834.470 Å with final percentual internal relative uncertainties. We indicate with “×” symbol the indices that were not used in the PCA regression. The full version is available as supplementary material.

ID	λ_i (Å)	λ_f (Å)	$\sigma_{\text{final}}^{\text{rel}}$	ID	λ_i (Å)	λ_f (Å)	$\sigma_{\text{final}}^{\text{rel}}$ (Å)	ID	λ_i (Å)	λ_f (Å)	$\sigma_{\text{final}}^{\text{rel}}$
$i1^\times$	8390.170	8392.852	0.20	$i76$	8579.369	8581.406	0.15	$i151$	8774.903	8777.156	0.50
$i2^\times$	8392.852	8395.796	0.14	$i77$	8581.406	8582.777	0.11	$i152$	8777.156	8779.373	0.18
$i3^\times$	8395.796	8399.997	0.07	$i78$	8582.777	8583.871	0.13	$i153$	8779.373	8782.086	0.28
$i4^\times$	8399.997	8401.949	0.12	$i79$	8583.871	8585.048	0.21	$i154$	8782.086	8783.529	0.27
$i5^\times$	8401.949	8405.622	0.18	$i80$	8585.048	8587.833	0.20	$i155$	8783.529	8785.283	0.30
$i6^\times$	8405.622	8408.070	0.23	$i81$	8587.833	8589.910	0.21	$i156$	8785.283	8788.175	0.29
$i7^\times$	8408.070	8411.035	0.17	$i82$	8589.910	8595.833	0.18	$i157$	8788.175	8791.172	0.30
$i8^\times$	8411.035	8413.815	0.05	$i83$	8595.833	8597.521	0.19	$i158$	8791.172	8795.837	0.18
$i9^\times$	8413.815	8415.469	0.28	$i84$	8597.521	8600.498	0.14	$i159$	8795.837	8799.763	0.39
$i10^\times$	8415.469	8418.413	0.12	$i85$	8600.498	8601.953	0.22	$i160$	8799.763	8802.237	0.10
$i11^\times$	8418.413	8421.854	0.13	$i86$	8601.953	8604.931	0.21	$i161$	8802.237	8803.944	0.11
$i12^\times$	8421.854	8423.765	0.10	$i87$	8604.931	8607.399	0.23	$i162$	8803.944	8805.366	0.10
$i13^\times$	8423.765	8425.526	0.13	$i88$	8607.399	8609.319	0.26	$i163$	8805.366	8808.375	0.05
$i14^\times$	8425.526	8427.743	0.03	$i89$	8609.319	8610.403	0.19	$i164$	8808.375	8812.309	0.18
$i15^\times$	8427.743	8429.463	0.18	$i90$	8610.403	8613.631	0.09	$i165$	8812.309	8817.409	0.28
$i16^\times$	8429.463	8430.940	0.20	$i91$	8613.631	8618.739	0.14	$i166$	8817.409	8820.584	0.25
$i17^\times$	8430.940	8432.396	0.21	$i92$	8618.739	8620.138	0.23	$i167$	8820.584	8823.114	0.12
$i18^\times$	8432.396	8436.829	0.02	$i93$	8620.138	8622.354	0.14	$i168$	8823.114	8826.059	0.05
$i19^\times$	8436.829	8440.270	0.06	$i94$	8622.354	8627.392	0.20	$i169$	8826.059	8830.919	0.15
$i20$	8440.270	8445.199	0.09	$i95$	8627.392	8629.836	0.20	$i170$	8830.919	8834.470	0.26
$i21$	8445.199	8449.885	0.10	$i96$	8629.836	8631.937	0.22				
$i22$	8449.885	8451.508	0.07	$i97$	8631.937	8635.377	0.16				
$i23$	8451.508	8454.517	0.07	$i98$	8635.377	8638.090	0.23				
$i24$	8454.517	8456.237	0.06	$i99$	8638.090	8640.34	0.21				
$i25$	8456.237	8458.719	0.05	$i100$	8640.34	8643.583	0.21				
$i26$	8458.719	8461.663	0.08	$i101$	8643.583	8646.943	0.24				
$i27$	8461.663	8466.315	0.11	$i102$	8646.943	8649.393	0.19				
$i28$	8466.315	8471.245	0.05	$i103$	8649.393	8653.064	0.17				
$i29$	8471.245	8473.693	0.08	$i104$	8653.064	8658.494	0.15				
$i30$	8473.693	8475.182	0.08	$i105^\times$	8658.494	8666.718	0.05				
$i31$	8475.182	8477.896	0.11	$i106$	8666.718	8669.528	0.15				
$i32$	8477.896	8479.086	0.10	$i107$	8669.528	8671.017	0.23				
$i33$	8479.086	8480.575	0.10	$i108$	8671.017	8672.241	0.19				
$i34$	8480.575	8482.030	0.09	$i109$	8672.241	8673.962	0.22				
$i35$	8482.030	8483.751	0.09	$i110$	8673.962	8676.410	0.06				
$i36$	8483.751	8485.008	0.11	$i111$	8676.410	8677.634	0.31				
$i37$	8485.008	8486.265	0.11	$i112$	8677.634	8680.372	0.26				
$i38$	8486.265	8489.429	0.11	$i113$	8680.372	8682.300	0.25				
$i39$	8489.429	8492.109	0.13	$i114$	8682.300	8685.496	0.14				
$i40$	8492.109	8494.821	0.10	$i115$	8685.496	8687.480	0.15				
$i41$	8494.821	8496.311	0.06	$i116$	8687.480	8690.203	0.05				
$i42^\times$	8496.311	8499.288	0.03	$i117$	8690.203	8691.418	0.17				
$i43$	8499.288	8501.703	0.07	$i118$	8691.418	8693.370	0.10				
$i44$	8501.703	8503.266	0.10	$i119$	8693.370	8694.594	0.16				
$i45$	8503.266	8508.076	0.09	$i120$	8694.594	8695.818	0.14				
$i46$	8508.076	8509.565	0.12	$i121$	8695.818	8696.847	0.18				
$i47$	8509.565	8511.285	0.11	$i122$	8696.847	8698.531	0.16				
$i48$	8511.285	8513.271	0.11	$i123$	8698.531	8700.482	0.12				
$i49$	8513.271	8514.726	0.03	$i124$	8700.482	8702.965	0.18				
$i50$	8514.726	8517.083	0.08	$i125$	8702.965	8704.903	0.19				
$i51$	8517.083	8522.137	0.07	$i126$	8704.903	8707.893	0.19				
$i52$	8522.137	8523.361	0.09	$i127$	8707.893	8709.337	0.20				
$i53$	8523.361	8525.313	0.10	$i128$	8709.337	8712.546	0.11				
$i54$	8525.313	8527.034	0.09	$i129$	8712.546	8715.227	0.13				
$i55$	8527.034	8529.238	0.11	$i130$	8715.227	8716.715	0.13				
$i56$	8529.238	8530.958	0.12	$i131$	8716.715	8718.171	0.13				
$i57$	8530.958	8533.142	0.10	$i132$	8718.171	8720.421	0.15				
$i58$	8533.142	8535.855	0.09	$i133$	8720.421	8723.101	0.18				
$i59$	8535.855	8539.563	0.08	$i134$	8723.101	8726.066	0.16				
$i60^\times$	8539.563	8543.961	0.03	$i135$	8726.066	8728.514	0.21				
$i61$	8543.961	8545.945	0.05	$i136$	8728.514	8732.683	0.16				
$i62$	8545.945	8549.374	0.07	$i137$	8732.683	8736.854	0.11				
$i63$	8549.374	8551.095	0.12	$i138$	8736.854	8739.796	0.14				
$i64$	8551.095	8553.543	0.13	$i139$	8739.796	8742.277	0.18				
$i65$	8553.543	8556.365	0.14	$i140$	8742.277	8744.713	0.22				
$i66$	8556.365	8557.745	0.16	$i141$	8744.713	8746.201	0.23				
$i67$	8557.745	8561.681	0.13	$i142$	8746.201	8748.636	0.13				
$i68$	8561.681	8563.634	0.14	$i143$	8748.636	8752.091	0.16				
$i69$	8563.634	8565.089	0.18	$i144$	8752.091	8754.075	0.24				
$i70$	8565.089	8569.047	0.17	$i145$	8754.075	8757.979	0.14				
$i71$	8569.047	8572.487	0.14	$i146$	8757.979	8759.700	0.32				
$i72$	8572.487	8574.048	0.17	$i147$	8759.700	8764.617	0.17				
$i73$	8574.048	8575.135	0.15	$i148$	8764.617	8769.051	0.15				
$i74$	8575.135	8577.385	0.18	$i149$	8769.051	8770.989	0.33				
$i75$	8577.385	8579.369	0.20	$i150$	8770.989	8774.903	0.11				

Table A2. Column 1 lists the variables, i.e., color and spectral indices. Columns 2 and 3 list the mean and standard deviation used to normalize the variables in the form $\text{Variable}_j^{\text{norm}} = (\text{Variable}_j - \text{Mean}_j) / \text{Std}_j$ – in order to get a variables' distribution with 0 and 1 mean and standard deviation, respectively. Columns 4, 5, 6 and 7 list the coefficients derived by the PCA regression that, being multiplied by the normalized variables' vector, create the Principal Components. The full version is available as supplementary material.

Variable	Mean	Std	PC1	PC2	PC3	PC5
<i>J - H</i>	0.59443182	0.04552709	0.017392992	-0.042049815	0.487154363	0.3637667876
<i>i20</i>	0.40671511	0.25811607	-0.082275196	0.102241666	-0.011264184	-0.0396752735
<i>i21</i>	0.34567894	0.23123022	-0.082916601	0.091045205	0.0219376739	-0.0431499682
<i>i22</i>	0.16982121	0.06566573	-0.081422918	0.09004488	0.0974459883	-0.0275029256
<i>i23</i>	0.33903625	0.22863852	-0.08016789	0.129052651	-0.001602449	-0.0585099458
<i>i24</i>	0.17617413	0.11276828	-0.080625134	0.123963189	0.0268581814	-0.0767561055
<i>i25</i>	0.28391504	0.16430488	-0.081562147	0.114327971	0.0205351021	-0.03033259
<i>i26</i>	0.2766045	0.18470607	-0.082831315	0.097593103	-0.0156747225	-0.01811320588
<i>i27</i>	0.43927773	0.29521656	-0.081657078	0.107551106	-0.0069125349	-0.0797381373
<i>i28</i>	0.73391553	0.29109171	-0.083897916	0.074563686	0.0331092506	-0.0454053418
<i>i29</i>	0.28032803	0.18112735	-0.082024002	0.107233962	-0.0142134392	-0.0176886425
<i>i30</i>	0.14192388	0.10282675	-0.082282485	0.105699632	0.0040490258	-0.0274885583
<i>i31</i>	0.25109636	0.18126266	-0.082574778	0.103206163	0.0033750912	-0.0043288407
<i>i32</i>	0.11171872	0.07570451	-0.082989697	0.09634329	0.0173748786	-0.0293256437
<i>i33</i>	0.13897736	0.09498492	-0.082386003	0.103695897	0.037052364	-0.0318980012
<i>i34</i>	0.14980371	0.0956114	-0.082305235	0.100722106	0.0326366776	-0.0625237795
<i>i35</i>	0.17474708	0.10675363	-0.082510201	0.099295606	0.040152503	-0.0817328513
<i>i36</i>	0.10638822	0.07583941	-0.082097577	0.107864225	0.0130254591	-0.0592137083
<i>i37</i>	0.1156355	0.07917762	-0.082569833	0.100782138	-0.0032514927	-0.0348488209
<i>i38</i>	0.28822427	0.1922289	-0.083776641	0.084411983	-0.0057537133	-0.0567331916
<i>i39</i>	0.2207851	0.15017105	-0.084171267	0.07352147	-0.0159738402	-0.0358892318
<i>i40</i>	0.26158848	0.14448136	-0.083649013	0.06086956	0.0017600052	-0.0636953339
<i>i41</i>	0.2106442	0.07901366	-0.08425531	0.054744858	0.0648456553	-0.0071138349
<i>i43</i>	0.27783231	0.12258709	-0.085013136	0.051253744	0.0320752936	-0.0191469705
<i>i44</i>	0.15309916	0.08841463	-0.084603989	0.061560708	0.022897678	-0.0662439206
<i>i45</i>	0.5406636	0.34914814	-0.083736937	0.084893685	-0.0057156965	-0.0334389763
<i>i46</i>	0.14953586	0.1084143	-0.083462408	0.089172534	-0.0167264217	0.0108811494
<i>i47</i>	0.17242562	0.11910837	-0.083636857	0.077447803	-0.0001118251	0.0346563557
<i>i48</i>	0.20924455	0.12814084	-0.083538627	0.072587657	0.0382135558	-0.027667984
<i>i49</i>	0.29767027	0.0671156	-0.081448631	0.039347755	0.1675914636	-0.1192314997
<i>i50</i>	0.32637413	0.16502801	-0.082371403	0.100934161	0.0663593605	-0.035202341
<i>i51</i>	0.6736822	0.33799078	-0.082831609	0.098841273	0.0474689276	-0.0363919954
<i>i52</i>	0.13360598	0.08657209	-0.082013961	0.111101215	0.0202782809	-0.0422074209
<i>i53</i>	0.19331083	0.12564916	-0.083007992	0.098445338	0.0303926288	-0.0307451552
<i>i54</i>	0.19902754	0.10392635	-0.082987935	0.082269989	0.0938319146	-0.0333006905
<i>i55</i>	0.22834189	0.13862311	-0.083334072	0.092674914	0.0204756515	-0.0439372845
<i>i56</i>	0.18343598	0.10958116	-0.083385953	0.092120643	0.0203166122	-0.0335679888
<i>i57</i>	0.23967167	0.13125559	-0.083917417	0.080302744	0.0332116875	-0.0240026929
<i>i58</i>	0.30578773	0.14822983	-0.084651265	0.061866683	0.0205812602	-0.0133720491
<i>i59</i>	0.56545909	0.14626777	-0.083609819	-0.004036885	0.1059674321	-0.0414764408
<i>i61</i>	0.35938996	0.0594687	-0.076747366	-0.064698363	0.1779508297	-0.0213651654
<i>i62</i>	0.4666589	0.13878976	-0.084022835	-0.005341379	0.0794070289	-0.0058885972
<i>i63</i>	0.17247625	0.08503004	-0.085408022	0.025239784	0.0112918046	-0.0058620395
<i>i64</i>	0.22881712	0.13116281	-0.085196157	0.039568153	-0.020046792	0.0163914135
<i>i65</i>	0.258110515	0.1503115	-0.085683392	0.030950981	0.0072631479	-0.000230114
<i>i66</i>	0.11290471	0.07085985	-0.085125589	0.02937078	0.0194240275	0.0118715837
<i>i67</i>	0.42480409	0.26700952	-0.085376442	0.053392493	-0.017039493	-0.0117187421
<i>i68</i>	0.18615992	0.12043932	-0.085484332	0.0481424	-0.0098387536	-0.0073821227
<i>i69</i>	0.12522229	0.08459503	-0.08529374	0.048980084	-0.0194800051	0.0035443405
<i>i70</i>	0.3313336	0.2225693	-0.085587777	0.037453701	-0.014208587	0.0239196918
<i>i71</i>	0.337685	0.21149735	-0.085443237	0.048544178	-0.0072350343	0.0221100044
<i>i72</i>	0.14513782	0.09656165	-0.085299948	0.047476406	-0.025310022	0.0158300183
<i>i73</i>	0.1007517	0.06500711	-0.085681466	0.03270413	0.0039079475	0.0216945445
<i>i74</i>	0.18967881	0.12790317	-0.085540173	0.03238452	-0.0229149245	0.0267455125
<i>i75</i>	0.16195949	0.10910287	-0.085578265	0.035349095	-0.0129149776	0.0371118815
<i>i76</i>	0.1805003	0.12677026	-0.085447085	0.046934136	-0.026258472	0.0157692041
<i>i77</i>	0.17198193	0.06949543	-0.085052113	0.003178242	0.0913985651	0.05774963
<i>i78</i>	0.11141617	0.05873708	-0.085150862	0.03029419	0.0483528909	0.0638639443
<i>i79</i>	0.10197177	0.07042437	-0.085199173	0.04578849	-0.013454654	0.052824858
<i>i80</i>	0.22011418	0.15613495	-0.085321085	0.043226164	-0.0191665521	0.0203567645
<i>i81</i>	0.16815323	0.11673784	-0.085381178	0.03367642	-0.0214518198	0.0636497568
<i>i82</i>	0.51671208	0.3461347	-0.08539129	0.035407955	-0.0123373715	0.0513233678
<i>i83</i>	0.13415504	0.09485464	-0.085209877	0.033157009	-0.0066489261	0.0866009065
<i>i84</i>	0.25111545	0.15055119	-0.085406906	0.017561489	0.0302995219	0.087476817
<i>i85</i>	0.11461999	0.07090896	-0.085278047	0.029268181	-0.0120657492	0.0585266968
<i>i86</i>	0.21697517	0.15835267	-0.085508824	0.027742012	-0.0011432453	0.0806874066
<i>i87</i>	0.17528893	0.13133744	-0.085690722	0.020736893	-0.0139773827	0.082355655
<i>i88</i>	0.12458028	0.09819802	-0.085466329	0.021322793	-0.0056088681	0.0982505503
<i>i89</i>	0.07009203	0.05384342	-0.085373352	0.02033012	0.0311285425	0.056616093
<i>i90</i>	0.35107481	0.155991	-0.08592485	-0.001378498	0.0490261307	0.038507224
<i>i91</i>	0.40714337	0.27731662	-0.086304055	0.003863258	-0.0019279218	0.0096802999
<i>i92</i>	0.09819069	0.07729978	-0.085938524	0.004431976	-0.0194661584	0.0694594886
<i>i93</i>	0.18691186	0.09780898	-0.085058813	-0.022062821	0.064659784	0.0785997954
<i>i94</i>	0.34259916	0.26389809	-0.085779871	0.025161904	0.0149124415	0.036730694
<i>i95</i>	0.1741404	0.13177024	-0.085303701	0.034895397	0.0154393849	0.0141977337

Variable	Mean	Std	PC1	PC2	PC3	PC5
i96	0.14986292	0.11239392	-0.085530254	0.038687116	0.0236438043	0.0015332313
i97	0.25146989	0.15548816	-0.084746459	0.017098309	0.0735126637	0.0529481037
i98	0.16671691	0.12586519	-0.084801798	0.033993351	0.050251354	0.0560871347
i99	0.16163798	0.1212219	-0.08511923	0.037569575	0.0170764249	0.0020455354
i100	0.19308294	0.14574406	-0.0841996	0.030821975	0.0616532279	0.0850513918
i101	0.24536052	0.17649419	-0.084808437	0.044098522	0.0129914758	0.0557515932
i102	0.17845078	0.11989134	-0.084964086	0.034510739	0.0593092182	0.0269608975
i103	0.30263447	0.17886801	-0.085030855	0.033735714	0.0372890386	0.0308712062
i104	0.48917443	0.23093181	-0.084847443	-0.046249202	0.0110871613	0.082376765
i106	0.25341837	0.1199623	-0.083846875	-0.057183794	-0.0051843858	0.1057328852
i107	0.10881087	0.06487943	-0.08338185	-0.058387588	-0.0187403112	0.1134804373
i108	0.09347712	0.05517833	-0.08385096	-0.059115886	-0.0001335588	0.0960615466
i109	0.13286617	0.08000828	-0.084566686	-0.048754265	-0.0132525346	0.0994285892
i110	0.39899034	0.09475892	-0.079051851	-0.118830695	0.0569024501	0.0929194081
i111	0.08174456	0.05610179	-0.083883088	-0.056415405	-0.0659383089	0.0894565046
i112	0.1917222	0.12320819	-0.084421395	-0.046238828	-0.0128747296	0.1108493317
i113	0.14497502	0.09163848	-0.084909902	-0.045628514	-0.0395547632	0.0872115705
i114	0.32554981	0.13853283	-0.083561118	-0.078211888	-0.0322393115	0.0708668027
i115	0.17619167	0.08793204	-0.082343702	-0.09577231	0.0127919372	0.0827291882
i116	0.62655852	0.09989846	-0.068484376	-0.18107765	0.1731441551	-0.0125561895
i117	0.11495466	0.06140391	-0.083424169	-0.070461809	-0.0162091662	0.0255055757
i118	0.25455739	0.09924167	-0.083782617	-0.046954947	0.0003919154	-0.0198085932
i119	0.12906973	0.07324856	-0.08477769	0.001276274	-0.0177803436	0.0051510911
i120	0.13330996	0.07231874	-0.084272988	0.001289059	-0.0160397648	-0.0402312173
i121	0.08700899	0.05544443	-0.085000738	0.001366778	0.0033414296	-0.0058640567
i122	0.15875174	0.09010921	-0.084127665	-0.004457592	0.0148194225	-0.0579998981
i123	0.17666765	0.08926536	-0.083563734	-0.034959217	0.0945905172	-0.0002001871
i124	0.20206178	0.12420656	-0.085025307	-0.013641296	0.0106194457	-0.0024370258
i125	0.13402992	0.08834963	-0.085121241	-0.032991536	-0.001239109	0.0138052988
i126	0.22038208	0.14499373	-0.085386265	-0.022426864	-0.0096335616	0.0287389188
i127	0.09458858	0.06719556	-0.084079784	-0.037819577	-0.014904956	0.0355566893
i128	0.3222128	0.17578936	-0.083293241	-0.047914507	0.0150744289	-0.0362613132
i129	0.25371985	0.13538776	-0.083534554	-0.050524035	0.0263859421	-0.0077108058
i130	0.14098875	0.08167171	-0.084359503	-0.015926074	-0.0242651826	-0.027729165
i131	0.13837667	0.07012221	-0.084320812	-0.03861794	0.0280314692	-0.0450300601
i132	0.20547015	0.11691041	-0.083825194	-0.037601267	-0.0080331835	-0.0279041358
i133	0.2035689	0.13954051	-0.084553022	-0.026431344	-0.0435087342	0.0102356766
i134	0.22630705	0.14891604	-0.08439553	-0.019851047	-0.015080093	-0.0331918392
i135	0.14485144	0.10269643	-0.083858716	-0.027535519	0.0105171787	-0.0063489142
i136	0.32670534	0.19054708	-0.084644459	-0.034204075	-0.0105706093	-0.0530043479
i137	0.42440284	0.18238542	-0.083550553	-0.084132632	0.0181960073	-0.0672251183
i138	0.2666453	0.150199	-0.08468076	-0.052538734	-0.0544165006	-0.0556925672
i139	0.19195314	0.10833321	-0.083481147	-0.082511863	-0.0361135984	-0.0778330341
i140	0.14168004	0.09815464	-0.082294754	-0.096145876	-0.0786394827	-0.020821101
i141	0.09165217	0.06351014	-0.082325465	-0.084849193	-0.0799766491	-0.0216610276
i142	0.22090064	0.11881728	-0.083492197	-0.075933668	-0.055982219	-0.0499344981
i143	0.2632828	0.16096411	-0.08378071	-0.077209399	-0.0661129701	-0.0537634925
i144	0.12137028	0.08264403	-0.080940723	-0.108901315	-0.0900960891	-0.0518953711
i145	0.36233049	0.16467008	-0.081295782	-0.110222972	-0.0509945764	-0.0519368158
i146	0.08914297	0.0672808	-0.080436193	-0.106851794	-0.1079336937	-0.0547042879
i147	0.3239767	0.17990019	-0.079248737	-0.135378838	-0.0520803502	-0.0370343542
i148	0.35987273	0.19299453	-0.081134383	-0.078152306	-0.0907787291	-0.1136752872
i149	0.09972542	0.07369268	-0.079745333	-0.097967783	-0.1004904367	-0.0383242451
i150	0.36269583	0.10405323	-0.060609417	-0.221361588	0.0958686969	0.0399223204
i151	0.0704919	0.06600187	-0.067887449	-0.149690929	-0.1435433236	-0.0253037874
i152	0.19129848	0.09742386	-0.080517733	-0.078841029	-0.0795107163	-0.1389866999
i153	0.17840902	0.11412152	-0.081143341	-0.092831866	-0.1041369486	-0.0989746055
i154	0.09120272	0.05949992	-0.079309862	-0.106387255	-0.1338970962	-0.1194024543
i155	0.09642644	0.06441347	-0.077330977	-0.138100508	-0.0910398564	-0.045581462
i156	0.15225897	0.10992801	-0.078475988	-0.109140151	-0.1417457408	-0.1138915413
i157	0.15272985	0.09950162	-0.075569351	-0.14987268	-0.0855162457	-0.1271282305
i158	0.28520705	0.15322724	-0.073565773	-0.175505831	-0.0148461575	-0.0194874729
i159	0.12399451	0.1091634	-0.073941205	-0.154710841	-0.0845474408	0.0090121649
i160	0.23591307	0.11228714	-0.081897489	-0.056886754	-0.0432177179	-0.1340466739
i161	0.15845492	0.06399078	-0.080378105	-0.035588615	-0.0164507559	-0.2280334333
i162	0.14051186	0.02945819	-0.036437007	-0.214928539	0.3897321725	-0.1400835454
i163	0.5430053	0.07159714	0.006124041	-0.239369256	0.4123487509	-0.2892592607
i164	0.20169261	0.09786016	-0.079619896	-0.099657008	0.0100316874	-0.0060493658
i165	0.15598481	0.12440081	-0.076024864	-0.114346156	-0.0972785087	0.223420543
i166	0.12208871	0.07524293	-0.072318932	-0.121090722	-0.0490116832	0.3115270691
i167	0.18920061	0.08040957	-0.078791264	-0.093892474	-0.0232771606	0.0754791313
i168	0.45372708	0.076632	-0.059065689	-0.185273769	0.1339938814	-0.1005946349
i169	0.21973708	0.13867545	-0.075982408	-0.049627388	-0.0439245017	0.1301201449
i170	0.1183822	0.07988999	-0.073811453	-0.074450937	-0.0944692762	0.3062850656

ID	RA J2000	DEC J2000	$T_{\text{eff}}^{\text{PCA}}$ (K)	$\sigma T_{\text{eff}}^{\text{PCA}}$ (K)	$[\text{Fe}/\text{H}]^{\text{PCA}}$ (dex)	$\sigma[\text{Fe}/\text{H}]^{\text{PCA}}$ (dex)	RV (km/s)	σRV (km/s)	S/N	J,H 2MASS flag	Spt ^{SIMBAD}
HIP 79431	16:12:41.8	-18:52:31.7	3812	166	0.02	0.31	0.9	1.2	250	A,A	M3V
GJ 618b	16:20:03.2	-37:31:48.6	3547	246	-0.25	0.55	33.9	1.1	20	A,A	M5
GJ 618a	16:20:03.5	-37:31:45.0	3715	66	-0.19	0.11	31.5	0.3	260,230,270,110	A,A	M3V
HIP 80268	16:23:07.7	-24:42:34.0	3963	118	0.40	0.26	-31.4	2.0	160	A,A	M2V
HIP 80440	16:25:13.0	-21:56:14.2	3461	91	0.21	0.18	-57.8	0.9	100	A,A	M0V
HIP 82283	16:48:46.0	-15:44:19.9	3458	89	-0.16	0.17	-73.5	1.6	160	A,A	M1.5V _k
HIP 82817	16:55:28.8	-8:20:10.3	2813	100	1.64	0.17	8.4	0.77	310,190	E,E	M3.5Ve
HIP 82834	16:55:38.0	-32:04:03.3	3601	91	-0.03	0.17	-22.0	1.6	200	A,A	K8V _k
HIP 83599	17:05:13.8	-5:05:38.6	3356	66	-0.08	0.13	38.2	1.1	300,280	A,A	M1.5V
HIP 84051	17:10:59.2	-52:30:56.0	3356	88	0.26	0.17	10.7	1.2	140	A,A	M1V
HIP 84123	17:11:52.3	-1:51:05.7	3270	105	0.24	0.19	-107.7	2.6	110	A,A	M3V
NLTT 44470	17:16:20.6	-5:23:51.3	2831	128	0.09	0.25	-36.5	1.1	190	A,A	M4V
GJ 3999	17:17:45.3	-11:48:54.2	3562	546	-0.05	0.99	22.1	1.5	300	A,A	M3
HIP 85523	17:28:39.9	-46:53:42.5	3488	109	0.17	0.26	-0.1	0.6	210,150	A,A	M3V
HIP 85605	17:29:36.3	24:39:11.1	3261	97	-0.43	0.20	-18.9	3.4	170	A,A	-
HIP 85647	17:30:11.2	-51:38:13.2	3844	92	0.10	0.17	-43.9	1.5	200	A,A	M0V
HIP 86057	17:35:13.6	-48:40:51.0	3721	103	-0.15	0.23	-17.1	0.7	120	A,A	M3V
HIP 86214	17:37:03.7	-44:19:08.8	3903	225	0.09	0.54	-43.3	1.4	120	A,A	M3.5
HIP 86961	17:46:12.8	-32:06:08.9	3702	76	0.28	0.16	-15.9	1.2	230,130	A,A	M1.5
HIP 86963	17:46:14.4	-32:06:08.2	3642	86	0.01	0.15	-22.7	0.7	180,130,230	A,A	M2.5
LTT 7077	17:46:29.3	-8:42:36.2	3175	188	-0.29	0.38	-16.6	2.0	190	A,A	M3.5
CD 57-6997	17:46:29.3	-57:19:24.3	3922	90	0.38	0.18	57.7	2.3	170	A,A	-
HIP 86990	17:46:34.3	-57:19:08.1	4011	105	0.45	0.20	-45.1	0.4	130,170	A,A	M3.5V
LTT 7246	18:15:12.4	-19:24:06.4	3242	112	-0.12	0.22	34.0	1.3	280	A,A	M2
GJ 714	18:30:12.0	-58:16:27.5	3287	93	0.20	0.21	-7.2	1.2	190	A,A	M1V
HIP 91608	18:40:57.3	-13:22:45.6	3821	92	0.08	0.20	-33.8	1.5	230	A,A	M1
LHS 5341	18:43:07.0	-54:36:48.2	3415	186	-0.49	0.35	16.6	1.0	170	A,A	M5
LTT 7419	18:43:12.5	-33:22:46.3	4010	88	0.45	0.17	-10.8	1.7	220	A,A	M2
GJ 4074	18:45:57.5	-28:55:53.3	3834	228	0.11	0.53	-25.7	2.3	190	A,A	M4
HD 175224	18:57:30.6	-55:59:30.2	3458	66	-0.18	0.16	-20.0	0.7	200,160	A,A	K5Ve+K7Ve
HIP 93206	18:59:07.5	-48:16:28.0	3935	172	0.05	0.33	-5.0	1.5	260	A,A	M4V
HIP 94739	19:16:42.9	-45:53:21.4	3715	89	-0.14	0.17	-37.8	1.7	240	A,A	M0V _k
GJ 754	19:20:48.0	-45:33:28.3	3531	220	-0.12	0.29	3.2	2.4	200	A,A	M4.5
HIP 99701	20:13:53.4	-45:09:50.6	3364	113	0.04	0.44	-26.0	1.0	150,690	A,D	M0V
HIP 100490	20:22:41.9	-58:17:08.4	3728	87	-0.08	0.16	1.8	1.9	220	A,A	M1V
L 210-70	20:27:42.1	-56:27:26.2	3540	220	0.04	0.41	-22.7	2.4	180	A,A	M2.5
HIP 102235	20:42:57.1	-18:55:04.8	3473	92	0.43	0.17	1.7	1.8	220	A,A	M1.5
HIP 102409	20:45:09.5	-31:20:26.7	3569	50	-0.10	0.10	-2.0	1.0	340,530,270,170,310	A,A	M1VeBa1
GJ 810a	20:55:37.7	-14:02:07.8	3188	241	0.06	0.49	-136.8	2.0	190	A,A	M4V
HIP 105090	21:17:15.3	-38:52:02.2	3410	80	0.01	0.31	20.5	0.3	380,290,430,660,220	D,C	M1V
HIP 106106	21:29:36.7	17:38:35.4	3531	163	-0.20	0.33	-20.0	0.7	150	A,A	M3Ve
HIP 106255	21:31:18.6	-9:47:26.3	3149	246	-0.33	0.50	-51.2	2.2	130	A,A	M4.5V
HIP 106440	21:33:34.0	-49:00:32.4	3467	86	0.23	0.32	13.9	0.6	140,200,190,190,340	A,D	M2/3V
GJ 1263	21:46:40.4	00:10:23.4	3949	216	0.11	0.43	-23.4	1.6	180	A,A	M4
HIP 107705	21:49:05.9	-72:06:08.6	3742	90	0.60	0.16	-15.4	2.6	260	A,A	M1Ve
HIP 108569	21:59:34.8	-59:45:10.5	3657	98	0.05	0.21	11.3	1.8	190	A,A	M2V
HIP 108706	22:01:13.1	28:18:24.9	3341	192	-0.20	0.45	-3.5	3.3	110	A,A	M3.5Ve
GJ 4248	22:02:29.4	-37:04:51.2	3700	108	-0.13	0.23	-17.6	0.8	180,190	A,A	M3V
HIP 110534	22:23:33.3	-57:13:14.7	3364	62	-0.10	0.12	-2.7	0.9	100,230	A,A	M1V _k
GJ 9780	22:25:05.0	-47:52:46.2	3617	245	0.13	0.47	-9.9	2.2	170	A,A	M3.5
HIP 111766	22:38:29.7	-65:22:42.3	3348	131	-0.14	0.31	-7.0	1.4	160,180	A,A	M3Ve
GJ 866	22:38:33.7	-15:17:57.3	3480	305	0.16	0.46	6824.7	3.3	200	A,A	M5V
GJ 867b	22:38:45.3	-20:36:51.9	3536	111	-0.09	0.26	0.4	1.0	260,110	A,A	M3.5V
GJ 867a	22:38:45.6	-20:37:16.1	3487	64	-0.01	0.15	8.8	1.1	250,350,130	A,A	M0Vep
HIP 113229	22:55:45.3	-75:27:32.1	3832	166	0.13	0.35	65.1	0.9	170	A,A	M3V
HIP 113576	23:00:16.1	-22:31:27.6	3505	99	0.20	0.25	15.7	1.3	120	A,E	K7+V _k
HIP 114719	23:14:16.6	-19:38:39.4	3249	94	0.24	0.19	4.9	0.7	140	A,A	M0.5V _k
GJ 896b	23:31:52.4	19:56:13.8	3182	305	0.24	0.89	-1.3	3.1	40	A,A	M4Ve
HIP 117828	23:53:50.2	-75:37:57.5	3395	125	-0.39	0.25	-13.3	1.9	230	A,A	M3
HIP 117966	23:55:39.8	-6:08:32.8	3198	125	0.04	0.27	19.5	2.2	220	A,A	M2.5V _k